Die approbierte Originalversion dieser Diplom-/Masterarbeit ist in der Hauptbibliothek der Technischen Universität Wien aufgestellt und zugänglich.
http://www.ub.tuwien.ac.at
TU UB WIEN Universitätsbibliothek
The approved original version of this diploma or master thesis is available at the main library of the Vienna University of Technology.
http://www.ub.tuwien.ac.at/eng

Unterschrift BetreuerIn

TECHNISCHE UNIVERSITÄT WIEN

DIPLOMARBEIT

Reliability in power electronics for electric energy converters

ausgeführt am Institut für
Angewandte Physik
der Technischen Universität Wien

unter der Anleitung von
Ao.Univ.Prof. Dr. Martin Gröschl

in Kooperation mit dem
Austrian Institute of Technology
Electric Energy Systems

Dr. Johannes Stöckl
Dr. Friederich Kupzog

durch
Stefan Kitzler BSc.

Vienna, October 24, 2018

Unterschrift StudentIn

Acknowlegement

At first I would like to thank Ao.Univ.Prof. Dr.techn. Martin Gröschl for giving me the opportunity to write this master thesis at the Institute of Applied Physics, TU Wien. I also want to thank the Austrian Institute of Technology for the collaboration and in particular Dr.techn. Johannes Stöckl and Dr.techn. Friederich Kupzog for their great support and cooperation.

Abstract

To meet the challenges of nowadays reliability for renewable energy systems, the advancements of robustness validation and lifetime prediction for power electronic devices is an important subject. This thesis has done further progress by developing an implementation and considering three relevant aspects: an operation specific mission profile containing physical environment data as well as load and stress profiles, a system specific characterization and universal failure mechanism sourced modules. The study has focused on the AIT smart grid converter (ASGC) power electronic system. System characteristics have been evaluated and thermal models prepared since the investigated failure mechanisms of electrolytic capacitors and IGBT semiconductors are primarily driven by their temperature. A particularly innovation is the development of the bond-wire fatigue failure model with the use of the rainflow algorithm for the computation of thermal cycles. Based on the mission profile considering 2017's offline data of Vienna, Austria as the operation area for a photovoltaic converter, the results show the dominance of cosmic radiation failures of semiconductors for the prepared models. Nevertheless this mission profile contains only small loads and therefore provides slight stresses to the components. The use of further applications profiles would yield worthwhile information.

Kurzfassung

Um den aktuellen Herausforderungen von Zuverlässigkeit für erneuerbare Energiesysteme gerecht zu werden, sind ausgeklügelte Fehlerrobustheitsvalidierungen und Lebenszeitprognosen von Leistungselektronikgeräten notwendig. Diese Diplomarbeit hat einen weiteren Beitrag zum Fortschritt geleistet, indem neue Umsetzungen erarbeitet wurden, unter Berücksichtigung von drei wesentlichen Aspekten: ein Mission Profil von speziell auf den Einsatzbereich abgestimmten physikalischen Umgebungsdaten und Lastprofilen, eine Charakterisierung des festgelegten Systems und Module basierend auf allgemein bekannten Fehlermechanismen. Diese Untersuchung hat sich speziell auf das AIT Smart Grid Converter (ASGC) Leistungselektroniksystem bezogen. Die Systemcharakterisierung wurde evaluiert und daraus ein thermisches Modell erstellt, da die betrachteten Fehlermechanismen, sowohl der Elektrolyt Kondensatoren als auch der IGBT Halbleiterbauteile, vor allem von der Bauteiltemperatur abhängen. Besonders innovativ war in diesem Zusammenhang die Entwicklung des Modells für die Ermüdung der Halbleiterchips-Bauteilanschüsse, unter Verwendung des Rainflow-Algorithmus zur Berechnung von thermischen Zyklen. Unter Verwendung eines Mission Profiles aus dem Jahre 2017 mit offline Daten eines Photovoltaik Wechselrichters, Standort in Wien, Österreich, hat sich für das ausgearbeitete Modell die kosmische Strahlung als dominanter Ausfallsgrund gezeigt. Allerdings beinhalten diese Daten nur sehr geringe Belastungen für die Systembestandteile. Die Anwendung von weiteren Profilen und Messungen zur Systemcharakterisierung könnten daher zu einem Informationszuwachs führen.

Contents

1 Introduction **1**
1.1 Motivation . . . 1
1.2 State of the art in reliability . . . 2
1.3 Aim of the work . . . 3

2 Theory and failure mechanisms **5**
2.1 Basics of Weibull distribution . . . 5
2.2 Electrolytic capacitor failures caused by degradation effect . . . 7
2.3 Semiconductor failures caused by cosmic radiation . . . 10
2.4 Semiconductor failures caused by thermo-mechanical stress . . . 13

3 Modelling and implementation **16**
3.1 Mission profile . . . 17
3.2 System characterization and modelling of the inverter system . . . 20
3.2.1 AIT Smart Grid-Converter . . . 20
3.2.2 Measurement for system characterization . . . 22
3.2.3 Thermal model of the electrolytic capacitors . . . 26
3.2.4 Thermal model of the semiconductors . . . 32
3.3 Modules and simulation . . . 35
3.3.1 Modelling of fatigue processes based on time course . . . 36
3.3.2 Modelling of fatigue processes based on thermal cycles . . . 38
3.3.3 Monte Carlo simulation . . . 45

4 Analysis and discussion **47**
4.1 Electrolytic capacitor failures caused by degradation effect . . . 47
4.2 Semiconductor failures caused by cosmic radiation . . . 53
4.3 Semiconductor failures caused by thermo-mechanical stress . . . 57
4.4 Overall simulation results . . . 63

5 Summary, conclusion and outlook **64**

References **66**

1 Introduction

Reliability of power electronics has become an uprising topic due to its use in integrated devices which are widespread in diverse modern industry sectors. Especially renewable energy is inextricably linked with power electronics and its utilization of convert systems, transforming sustainably photovoltaic energy to alternating current for low voltage households.

Nowadays reliability is an continual process, starting already in the development and design phase and tries to prevent maintenance and consequential costs. To meet these challenges, this thesis contributes an advanced lifetime prediction for power electronic systems. In order to develop an implementation with universal usability but close to an actual application it has been spits into separate parts. For a close relation to real operation the photovoltaic power inverter system AIT Smart Grid-Converter (ASGC) has been used, characterised and analysed in order to create system specific models. These thermal models are driven by mission profile information, containing application and environment data of the system, and generate component data. This information is used in the second part of the implementation to generate failure probabilities based on three universal fatigue models. The implementation includes two semiconductors failure models and one for the electrolytic capacitors, representing the main and generalizable fatigue mechanisms for power electronic components. The simulation uses the failure probability for the Monte Carlo random experiments to provide a loss prediction.

In particular the development of the bond-wire degradation fatigue model has been an innovative process. The strategy and implementation of the rainflow algorithm as a thermal-cycle counting method and the merge with other simulations driven by time has been developed and will be discussed in this thesis.

The use of (offline) weather and low-voltage infrastructure information for the mission profile results in application-related data. Therefore the thesis provides a realistic perspective for component and system lifetimes and forms a basis for real-time screening, early diagnosis and predictive maintenance in modern reliability.

1.1 Motivation

The shift of conventional technologies to alternative electric solutions has expanded its range in moden industrial sectors like the automotive industries [44] and railway tractions [6] but especially in renewable and sustainable energy systems [21]. The future energy supply with 100% renewable energy is unthinkable without modern power electronic converters [20]. Compared to conventional synchronous machines, power electronic components are much more likely to fail. The essence of reliability engineering is to prevent the creation of failures. [37] Large-scale production and broadening of power electronic devices have increased the requirements in terms of safety, costs and reliability. [38] A transition can be seen in the costumer expectations of yesterday, today and the future. Yesterday's requirements have been in product and device warranty for years. But

since power electronic components have spread to safety sensitive operations areas, the challenge of today and the future requests predictive maintenance. [37] A blackout of power plants comes together with repair time and additional cost and may be critical in terms of power supply for households or infrastructure. Unfortunately the increasing penetration of renewable energy sources, failures become a bigger issues. Regarding [30], photovoltaic inverters are responsible for 37% of the unscheduled maintenances and 59% of the associated cost during five years of operation. [37] To prevent an outage, modern reliability is starting in the development process and continues in an ongoing real-time procedure: [37]

1. analytical analysis to understand the nature of power electronic failures;
2. design for reliability (DFR) and robustness validation [44] during development process;
3. intelligent control and condition monitoring using specific mission profiles, consisting of field operation data.

This trend provides scope for further development of analysis work, modelling and condition monitoring implementations.

1.2 State of the art in reliability

In the following a state of the art in reliability is given for the main research topics of this thesis. Nevertheless there are several great literature journeys and reviews like [37, 41, 42] that give a detailed insight and literature references.

Reliability engineering has started in the 1950s driven by the desire of the military caused by issues in electronic products. Various research streams have done pioneer work including quantitative reliability prediction or identifying the physics of failure (PoF) and modelling the physical causes of component failure. [37] Until the 1980s handbooks based on constant failure rates have been dominantly used for life time prediction, in particular the Military-Handbook-217 series (MIL) [2]. In the 1990s the increasing complexity of integrated circuits (ICs) suggested that constant failure rates are not adequate anymore. [37]

In the past years there have been several changes in the strategy of analysis and testing. The focus has shifted to the nature and physics of failure instead of considering only failure rates regarding the components. Therefore failure models under environment and stresses have been further advanced. Especially the electrolyte degreadation in capacitors [36] and bond-wire fatigue in IGBT modules [15, 40] for DC-link applications [38] have become a major subject in research. [37] This trend in PoF requires advanced acceleration testing, result analysis and modelling. [9,14] Another progress in reliablity has been made by the increasing usage of power electronic components in the industry. New methods have been initiated like Focus point matrix (FPM), as suggested in [44], to analyze critical stressors with the potential to kill components. [37] Together with PoF, the progression of robustness validation has been further increased. [38, 42] The

use of application specific mission profile approaches [43] have improved the weak point detection already in the design stage [24, 41] but also provides real-time prognosis and condition monitoring for cost effective predictive maintenance and lifetime prediction. [41, 43]

1.3 Aim of the work

To make a scientific contribution to nowadays power electronic system reliability, the aim of this thesis is to create a system specific implementation for robustness validation of design specification. By assuming state of the art fatigue mechanisms, the goal is to develop universal methods to analysis failures and predict lifetimes of electronic devices, in respect to further development and usage for condition monitoring and predictive maintenance.

The stress of power electronics devices is caused by their distinct operation but the failure mechanisms are universal effects and the issues can be reduced to several components. Figure 1 shows the failure root causes. [38]

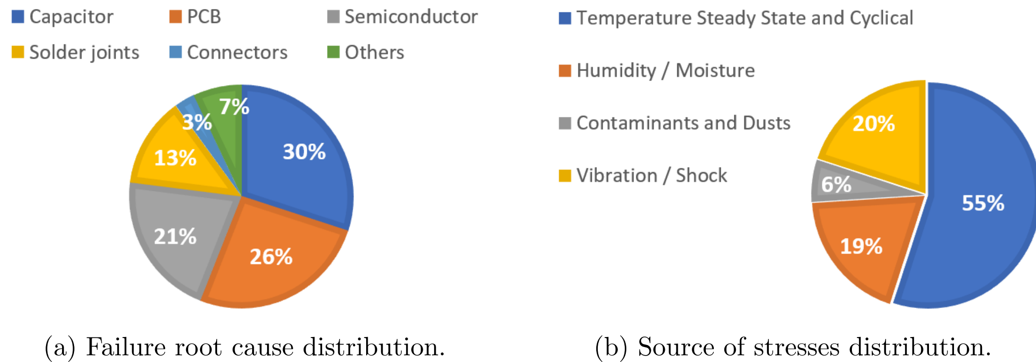

(a) Failure root cause distribution.

(b) Source of stresses distribution.

Figure 1: Failure and stress distributions in power electronic systems.

To meet the challenge of developing a universal method with versatilely usable in multiple operation fields but adjustable to each application field, the aim is a separating approach. Therefore it is meaningful to split the implementation into universal failure methods and specific system characteristic part.

The universal methods focus on the critical components of inverter systems which are the main weak points [10, 14, 38, 41]:

- the electrolytic capacities and
- the IGBT semiconductors.

Failure models provide probability to failure for the loss prediction. Non-existing models must be developed and available once adjusted and advanced. The focus for the implementation determines on three fatigue models:

- electrolyte degradation for electrolytic capacitors,
- semiconductor failure caused by cosmic radiation and
- semiconductor bond-wire fatigue caused by thermal swings.

Especially the development of the non-existent bond-wire degradation model is one of the main purposes in this work. The challenge is not only to create an approach to compensate the lack of power cycle acceleration-test results for semiconductors, but also to merge the results of simulations with different counting bases.

A system specific model acquired by thermal characterization measurement of the power inverter system AIT Smart Grid-Converter (ASGC) is the system specific part of this work. This model generates component data for the failure models driven by the mission profile.

Application adapted lifetime prediction base on mission profiles, which are the input of the simulation and contains the environment and operation data. Wear and reliability highly depend on the specific application field especially in renewable energies like photovoltaic. Applications vary in environment conditions and in particular on load intervals and intensity. Therefore the aim is to use mission profile based lifetime prediction in order to realise modern robustness validation for design specifications. Figure 2 shows a Weibull plot of example data and an exemplary schematics for the robustness validation.

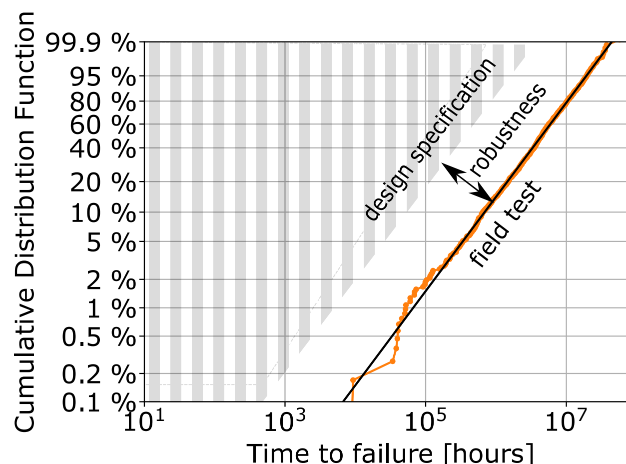

Figure 2: Exemplary schematic reliability Weibull plot of field test data and robustness validation for design specifications.

2 Theory and failure mechanisms

In this section the theoretical background of methods and processes will be described.

The failure mechanisms of power electronic devices can be subdivided into two categories, the extrinsic and intrinsic mechanisms. The extrinsic is the result of poorly controlled or poorly designed manufacturing processes. The intrinsic failure (wear-out) mechanisms are often the main reason for the limited lifetime of the power electronic devices caused by their operation close to the physical limits of material and device. [10, pp.225-228]

A very widely recognized graphic in reliability and lifetime is the bathtub curve. It has been originally designed to display the rate at which humans die according to their age but later on adopted to describe the lifetime of products. In Figure 3 the scheme is visualized with three distinct intervals.

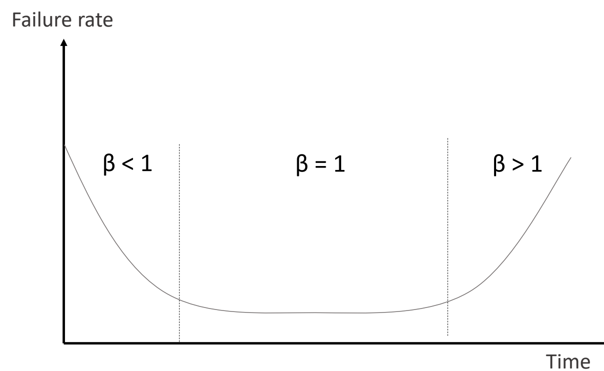

Figure 3: Bathtub curve.

In lifetime performance the bathtub curve for the failure rate can be separated into three sections:

1. Early failure period: decreasing failure rate ($\beta < 1$)
2. Random failure period: constant failure rate ($\beta = 1$)
3. Wear-out failure period: increasing failure rate ($\beta > 1$)

At first a high rate of early failures is caused by material weakness or variation in quality of the manufacturing process. The second part is called the useful lifetime because failures occur only randomly. The manufacturer usually tries to gain this phase. The third part is known as the wear out failures due to fatigue, attrition and ageing of the material. [28, pp.111-129]

2.1 Basics of Weibull distribution

The Weibull distribution has been introduced of the Swedish researcher Waloddi Weibull in 1939 to describe the theory of material fatigue. It turned out that

the distribution can be also be used in reliability and lifetime illustration for monotone increasing, constant and monotone decreasing failure rates. Nowadays it is general accepted to make use of the Weibull distribution for parameters which affect the lifetime like e.g. stress or force. [1,28]

A steady, none negative random variable is Weibull distributed, if the cumulative distribution function (cdf) or also called unreliability function is given by

$$F(t) = 1 - e^{-(\frac{t-t_0}{\eta})^\beta} \quad , \tag{2.1.1}$$

(2.1.2)

for $t > t_0$ and scale parameters β and η. η can be interpreted as a characteristical lifetime. In this thesis the parameter time t will also be replaced in some cases by the number of cycles n. Therefore η can be seen as a characteristical number of cycles. For $\beta = 1$, the Weibull distribution is equal to the exponential distribution but with a transformation of the parameters η. For $\beta = 2$ it transforms to the Rayleigh distribution. [1,28]

The reliability function of the distribution is simply one minus the cumulative distribution function

$$R(t) = 1 - F(t) = e^{-(\frac{t-t_0}{\eta})^\beta} \quad . \qquad [1,28] \tag{2.1.3}$$

The probability density function (pdf) is given by

$$f(t) = \frac{dF(t)}{dt} = \frac{\beta}{\eta} \times (\frac{t}{\eta})^{\beta-1} \times e^{-(\frac{t}{\eta})^\beta} \quad . \qquad [1,28] \tag{2.1.4}$$

In Figure 4 some pdf distribution examples for a variation of β-values are illustrated, which form sections of the bathtub curve.

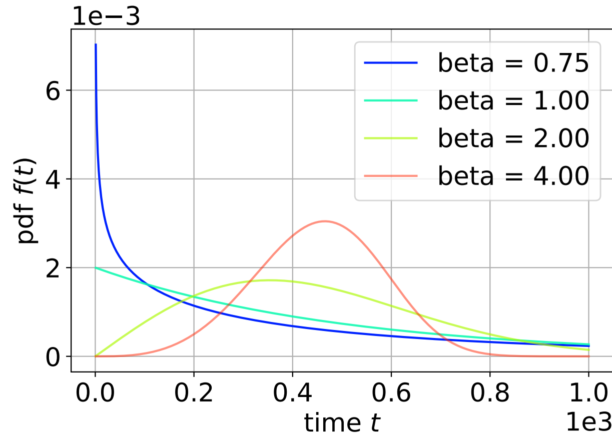

Figure 4: Weibull probability density function $f(t)$ for $\eta = 500$.

The failure rate of the Weibull distribution is given by

$$h(t) = \frac{f(t)}{R(t)} = \eta^{-\beta} \times \beta \times (t)^{\beta-1} \quad . \qquad [1,28] \tag{2.1.5}$$

Weibull plot is a special graphical illustration of Weibull distributed random samples, so that they are adjusted on a straight line. This procedure can be done in various ways but a straightforward solution is the median rank for the plot preparation. The sorted random samples (e.g. failure times) can be ranked by

$$MR \sim \frac{i - 0.3}{N + 0.4} \times 100, \tag{2.1.6}$$

where i is the (failure) order number and N the total sample size.

Taking the natural logarithm twice, reduces the Weibull cdf into a linear equation $y = k \times x + d$:

$$F(t) = 1 - e^{-(\frac{t-t_0}{\eta})^\beta} \tag{2.1.7}$$

$$-ln(1 - F(t)) = (\frac{t - t_0}{\eta})^\beta \tag{2.1.8}$$

$$\underbrace{ln(-ln(1 - F(t)))}_{y} = \underbrace{\beta \times ln(t - t_0)}_{k \times x} - \underbrace{\beta \times ln(\eta)}_{d} \quad . \tag{2.1.9}$$

By entering the approximated values MR into $F(t)$ yield the y-values of the linear equation. These y- and x-values form pairs of values on a straight line. These values can be used to visualize the sample in a Weibull plot. [1, 28]
In Figure 5 an example is illustrated.

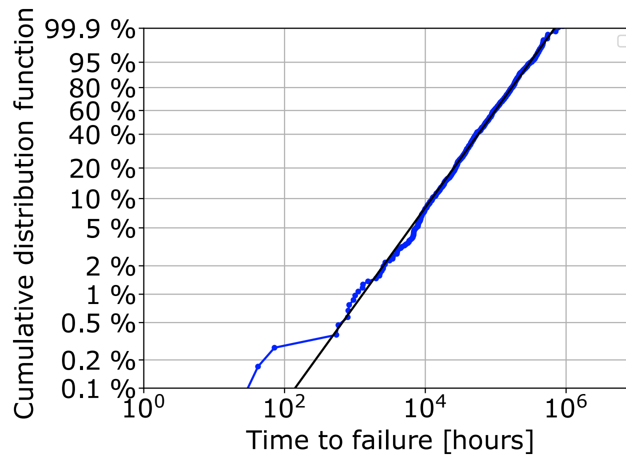

Figure 5: Example for Weibull plot.

Each point of the plot connects the operation time and the percent of failures.

2.2 Electrolytic capacitor failures caused by degradation effect

Electrolytic capacitors are widely used in power electronic devices to balance distinct input sources and output loads as well as for the reduction of voltage variations. Capacitors are passive elements of an electric circuit, their operations focuse on the supply of quick energy storage. The type of capacitors concerns

to the specific application and distinguishes between e.g. operation temperature, voltage and frequency. In general there are two types of electrolytic capacitos: aluminium electrolytic (Al-Caps) and solid tantalum. In this thesis the focus is on Al-Caps because solid tantalum capacitors are mainly used for applications below 100 V. [10]

In Figure 6 the principle model of the capacitor is shown.

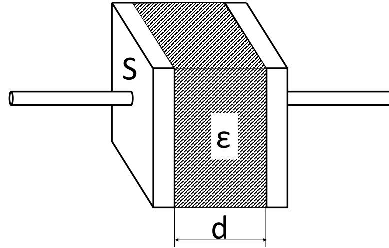

Figure 6: Basic scheme model of capacitor.

Regarding this structure the capacity can be calculated by

$$C = 8.855 \times 10^{-8} \, \frac{\epsilon S}{d} \, \mu\text{F} \quad , \tag{2.2.1}$$

with a dielectric constant ϵ, the dielectric surface area S in [cm^2] and the dielectric thickness d in [cm]. [32]

More precise the capacitor consists of a capacitor paper (electrolytic paper), an electrolyte and electrodes, wich are made of aluminum foil. The anode foil surface is covered with an oxide film. The thin oxide film offers the dielectric constant and forms in contact with the electrolyte isolation properties. The thickness of the dielectric is nearly proportional to the forming voltage with approximatly $1.3 \times 10^{-3} - 1.5 \times 10^{-3}\,\mu\text{m}\,\text{V}^{-1}$. [31]

In the reliability of Al-Cap the failure rates and useful lifetime can also be approximated by the bathtub curve, consisting of early, random and wear-out failures. [31] Focus for this thesis are the wear-out failures, defined as the following criteria [32]:

- Change in capacitance
- Dissipation factor $tan(\delta)$
- Leakage current

$$tan(\delta) = \frac{R}{1/(\omega C)} = \omega \, C \, R_{ESR} \quad . \tag{2.2.2}$$

Lifetime Estimation An aluminium electrolytic capacitor is determined to have reached its end of life when the capacitance change across a certain value. Factors that affect a capacitance change are external parameters (like temperature, humidity, vibration etc.) as well as applied voltage, current and signal form.

The electric current through the electrolyte is mediated by the movement of the ions. The increase of the electrolyte temperature leads to the decrease of the viscosity and therefore a lower electrical resistance R_{ESR}. [4] Therefore the most important factor in the capacitor lifetime is the temperature. The application of the capacitor in the DC-converter is characterized by a periodical charge and discharge, affected by the ripple current and the resulting in heat production. This causes a loss of electrolyte due to the diffusion through the rubber seal material, which finally leads to a decrease in capacitance and increase of $tan(\delta)$. [31]

The power loss caused by the ripple current I_{ripple} and the finite resistance R_{ESR} rises the capacitors surface temperature above the ambient to a point where the internal heat generation balances with the heat radiation

$$W_{elec} = W_{therm} \quad , \tag{2.2.3}$$

$$\text{with } W_{elec} = I_{ripple}^2 \times R_{ESR} \quad . \qquad [31] \tag{2.2.4}$$

In general heat transportation can be via heat radiation, convection or conduction. In this application the radiation is the dominante factor and can be described by the Stefan-Boltzmann's law:

$$W_{therm} = \epsilon \sigma A (T_{surface}^4 - T_{ambient}^4) = \beta_e \times A \times \Delta T_{surface} \quad . \tag{2.2.5}$$

Equation 2.2.3 reduces to

$$\Delta T_{surface} = (T_{surface} - T_{ambient}) = \frac{I_{ripple}^2 \times R_{ESR}}{\beta_e \times A} \quad . \tag{2.2.6}$$

With the thermal equivalent circuit models[1],

$$R_{th} \times (T_{core} - T_{surface}) = R_{th}^{inside} \times (T_{surface} - T_{ambient}) \quad , \tag{2.2.7}$$

$$\alpha = \frac{R_{th}}{R_{th}^{inside}} = \frac{(T_{surface} - T_{ambient})}{(T_{core} - T_{surface})} = \frac{\Delta T_{surface}}{\Delta T_{core}} \quad , \tag{2.2.8}$$

the core temperature is given by

[1]Foster Thermal Model

$$T_{core} = (T_{core} - T_{surface}) + T_{surface} \tag{2.2.9}$$

$$= (T_{surface} - T_{ambient}) \times \frac{R_{th}^{inside}}{R_{th}} + T_{surface} \tag{2.2.10}$$

$$= \Delta T_{surface} \frac{1}{\alpha} + \Delta T_{surface} + T_{ambient} \tag{2.2.11}$$

$$= (1 + \frac{1}{\alpha}) \frac{I_{ripple}^2 R_{ESR}}{\beta_e A} + T_{ambient} \quad . \qquad [4] \tag{2.2.12}$$

The electrochemical reactions at the dielectric layer (self-heating) and diffusion through the seal lead to a shift of the capacity value. The reaction rate can be described by the Arrhenius equation

$$k = A \times e^{-\frac{E_a}{k_b T}} \quad , \tag{2.2.13}$$

$$\ln k = \frac{-E_a}{k_b T} + lnA \quad . \tag{2.2.14}$$

The Arrhenius equation can be used to calculate the finite lifetime

$$\ln(\frac{L_x}{L_0}) = \frac{E_a}{k_b}(\frac{1}{T_{core}} - \frac{1}{T_{max}}) \quad , \tag{2.2.15}$$

with the base lifetime L_0 according to the maximum rated core temperature T_{max}.

$$\ln(L_x) = \frac{E_a}{k_b}(\frac{1}{T_{core}} - \frac{1}{T_{max}}) + ln(L_0) \qquad [32] \tag{2.2.16}$$

$$L_x = L_0 \times \exp(\frac{E_a}{k_b}(\frac{1}{T_{core}} - \frac{1}{T_{max}})) \tag{2.2.17}$$

$$= L_0 \times f_1(T_{core}, T_{max}) \quad . \tag{2.2.18}$$

The operation voltage V_o can be considered as well by an additional factor $f_2(V_o)$

$$L_x = L_0 \times f_1(T_{core}, T_{max}) \times f_2(V_o) \quad . \tag{2.2.19}$$

$$f_2 = (\frac{V_R}{V_o})^7 \quad , \tag{2.2.20}$$

with the maximum rated voltage V_R. [35]

2.3 Semiconductor failures caused by cosmic radiation

Already in 1962 the first appearance of semiconductor radiation failures have been identified, when the Telstar 1 communication satellite outage occurred as a

result of the exoatmosphere contamination caused by nuclear tests. This shows up a weak point which has been taken very serious by the U.S. military in order to protect and minimize the possibility to destroy or even disturb their space systems. Much effort has been made to understand the nature of radiation damage to semiconductor devices. [33, pp.391-410]

Environment radiation that affects semiconductors are, beside outer space radiation, nuclear reactors, radiation processing activities, nuclear weapons and controlled fusion facilities. [33, pp.391-410] But for this thesis only environment cosmic radiations have been considered.

At the beginning of the 90th, an unexpected and unknown failure of power electronic semiconductors was detected. The blocking ability of semiconductor device got lost. The damage allocated as a melting channel through the entire component structure. The spontaneous appearance of this failure was strange and no obvious indicator was identifiable e.g. increase of leaking current. A hint were results of an experiment, when a mismatch occurred between different location. The failure rates changed from six failures within 700 device hours to none, when the experiment location has been modified from the lab to a deeper situated salt mine. These results helped to proof that cosmic radiation was the root cause of the failures for power electronic devices under high voltage stress. [22]

The primary cosmic radiation consists of

- 87% protons,
- 12% alpha-particles and
- 1% heavy nuclei. [33]

The main source of particles up to 10^{10} eV is our sun. Particles up to 10^{16} eV are assumed to be erupted by a supernovae and up to 10^{18} eV the source is expected to be in our galaxy. Above this energy supernovae cannot explain the extreme energy. [22] But these high-energy cosmic particles typically collide with atmospheric molecules and therefore do not reach the surface of the earth directly.[2] The elastic and inelastic interaction [39] between primary particles and atom nuclei of the atmosphere initiates a variety of secondary high energy particles, whereby a single high-energy particle can create up to a thousand secondary particles. [22] A more detailed discussion about the nuclear basics of the cosmic radiation origins and the interaction with silicon is given in [18]. This particle shower finally arrives at the earth surface, can be detected and causes failures in semiconductor components. [22] The Austrian physicist Viktor Hess has discovered the cosmic radiation in 1912 and therefore got the Nobel Prize in physics in 1935. [39]
Investigation in [39] shows that all types of secondary particles and interactions, except of nucleons, have among others a too small cross section or too tiny energy transfer and therefore cannot cause a failure. The only probable particle type

[2] Nevertheless it should be mentioned that in space technology the primary high-energy particles can affect failures in semiconductor particles.

to cause a semiconductor failure are nucleons. In the appropriate energy range the coulomb interaction can be neglected, whence protons and nucleons behave equally. Admittedly the amount of neutrons which reach the earths surface are much higher, compared to protons. It is also much easier to shield protons due to their electric charge. Hence neutrons are more likely to cause semiconductor outages.

In Figure 7a the characteristic trapezoidal electrical field of a blocking semiconductor device is shown.

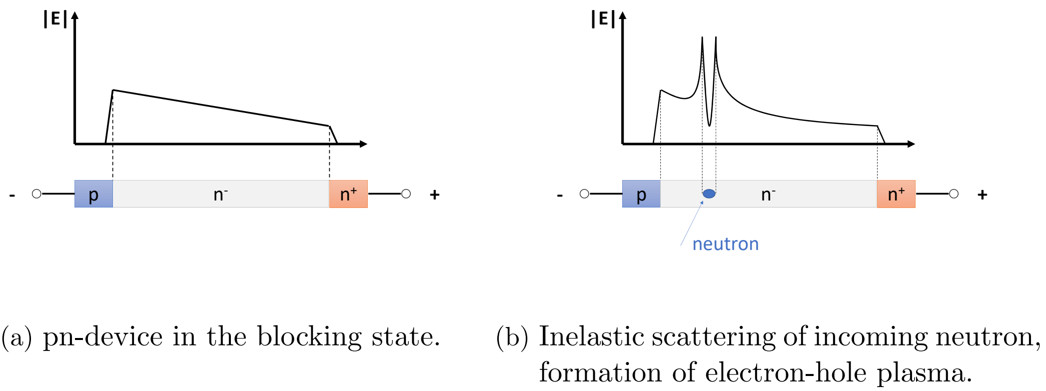

(a) pn-device in the blocking state.

(b) Inelastic scattering of incoming neutron, formation of electron-hole plasma.

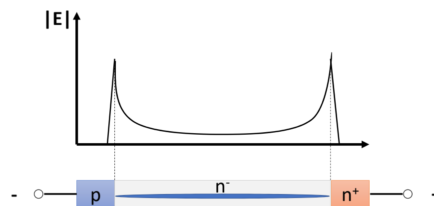

(c) Forming a streamer similar to a gas discharge.

Figure 7: Semiconductor destruction by neutron.

A neutron travelling through the space charge can be captured by a silicon lattice nucleus in a process of inelastic scattering. The strong interaction very likely initiates high-energy recoil ions in the range of 10 to 100 MeV, which generates lots of electron-hole pairs due to its propagation to the component. The electron-hole pairs in Figure 7b form a local plasma channel. In the plasma density of electrons and holes is high but the electric field is low. At the boarders between plasma and space charge, a very high peak due to a massive charge density emerges, up to 1 MV/cm for silicon. When the electric field reaches

a critical limit, carriers caused by ionization exceed the carrier flow out of the plasma region by diffusion. The result is a local current tube, similar to a gas discharge. This very high local current finally destroys the semiconductor device. [22, 39]

2.4 Semiconductor failures caused by thermo-mechanical stress

Although failures due to fatigue are typically associated with highly-stressed rotating machines, but vibration and thermal cycle affect contacts of electrical equipment as well. In particular metal suffers of this insidious issue, often unnoticed cracks propagating for some time and causes sudden and unexpected fractures. [33] The problems are often related to the chip packing. For advances power devices like IGBTs and MOSFETs, the packing concept has been further developed in order to host multiple chips in parallel. But this technology has now been generally accepted as a standard module design in power electronics. In Figure 8 the general concept has been illustrated. [22]

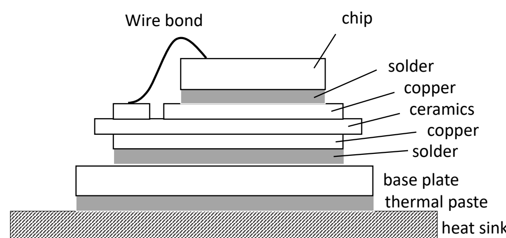

Figure 8: Schematic packing cross section for semiconductor.

The actual chip is located on the top of the packing structure on a solder and copper layers, connected with aluminium bond-wires to the copper tracks. More details of the structure, thickness and material of the layers are described in [22]. The different material specific coefficients of thermal expansion create mechanical stress at the interface due to thermal swings. For long operation time, these stresses cause the fatigue of materials and interconnections. The most common failure mechanisms are bond wire lift-off and solder fatigue, but these failure mechanisms are hardly separable in power cycling test. [23] Therefore, when in the following the failure mechanism is called bond wire lift-off, fatigue or degradation, solder fatigue has to be considered as well.

For the verification and evaluation of the fatigue mechanisms, controlled stress tests are performed for semiconductor components which are failure susceptible due to their high switching frequency .

The concept of these tests are to stress the power chips by cyclic thermal swing. In contrast to temperature cycling tests, the chips are self-heated by power loss. First the load current is conducted to heat up chip until a limitation temperature is reached. The chip is mounted on a heat sink as in real application. After

reaching the maximum temperature T_{high}, the load current is switched off again and the cooling system turns on. A temperature cycle is completed when the minimum (or start) temperature T_{low} has been reached again an the next cycle starts by starting the load current again. The swing temperature ΔT_j is given by the temperature difference

$$\Delta T_j = T_{high} - T_{low} \quad . \qquad [23] \tag{2.4.1}$$

In Figure 9 a power cycling example [17] is shown for 10% losses.

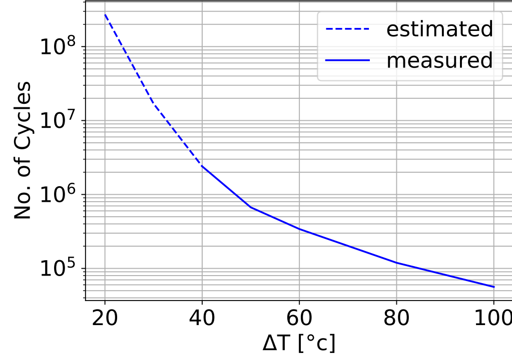

Figure 9: Example of Power cycle test results.

The power cycling curve provides loss information for a specific power electronic device by the relation of temperature gaps ΔT and the number of cycles. The first models for lifetime prediction have been implemented in the early 1990s with the LESIT project. [22] In this context an older formulation, the Coffin-Manson law, became relevant to introduce life time models.

Coffin-Manson is the a simple relation between the number of cycles to failure N_f and the temperature change ΔT. It has already been published in 1954 of L.F.Coffin [11] and S.S.Manson [25] independent of each other.

$$N_f = a \times (\Delta T)^{-n} \quad , \tag{2.4.2}$$

with empirical parameters a and n.

There have been several further developments and advanced approaches but for many applications this formulation is sufficient.
The Arrhenius approach is with an additional exponential factor

$$N_f = a \times (\Delta T_j)^{-n} \times e^{\frac{E_a}{k_b T_{j,m}}} \quad , \tag{2.4.3}$$

$$\text{with } T_{j,m} = \frac{T_{j,max} - T_{j,min}}{2} \tag{2.4.4}$$

as the mean temperature. [10]

Or the more precise model of Infineon's Bayerer [7] model.

In contrast to laboratory power cycling test considering constant and steady thermal gaps, in real operation a variation of different temperature swings take place. In previous models these distinct gaps have been added up to an accumulated damage by the use of the Miner's rule.

Miner's rule The Miner's rule is a linear damage hypothesis, which was popularised by M.A. Miner in 1945 [29] but earlier proposed by A. Palmgren in 1924. This is why it is also called the *Palmgren-Miner linear damage hypothesis*.

$$Q(\Delta T_j) = \frac{N(\Delta T_j)}{N_f(\Delta T_j)} \quad , \tag{2.4.5}$$

describes the linear accumulated damage piece by dividing the number of cycles $N(\Delta T_j)$ by the related number of cycles for a failure $N_j(\Delta T_j)$, regarding the temperature difference ΔT_j. By adding up the accumulated damage piece, the consumed lifetime can be evaluated. Certainly the model referees to a fixed critical damage limit, whence the lifetime ends with $Q = 1$. [22]

3 Modelling and implementation

Loss prediction based on mission profile data requires detailed modelling of the system and its essential fatigue mechanisms to obtain a lifetime simulation approach which is realistic. Separating the system characterization and the simulation of failures splits the implementation into a application specific and a universal part. In Figure 10 an overview of the implementation is given. All in all it represents the process structure: preparation - execution - analysis.

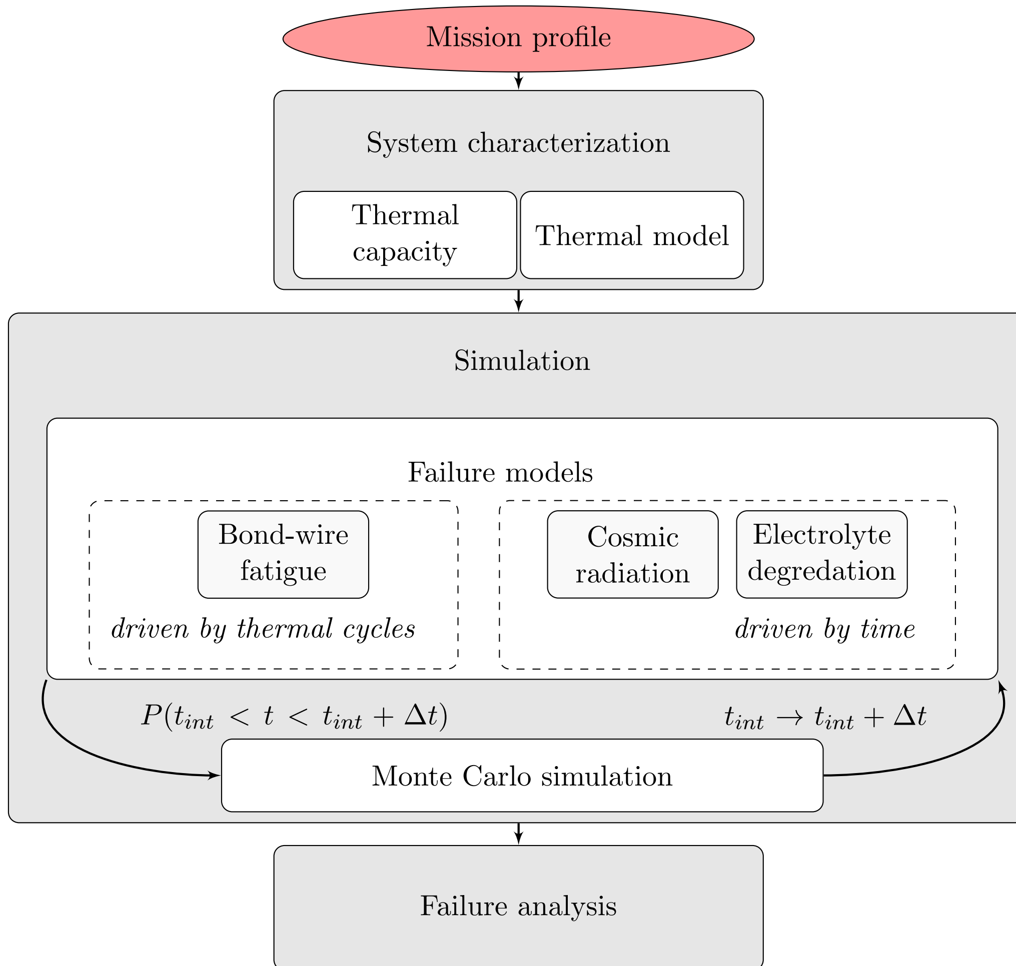

Figure 10: Flow diagram of the implementation, starting with the mission profile on the top. Seperation of inverter specific system charaterisation and independent simulation of the universal failure modes. At the bottom of the diagram the system failure analysis module process a preparation of the result and visualisation, which could also be outsourced.

A similar flow approach has been used in previous works [10,15] and is therefore widely accepted.

At the beginning of the procedure the mission profile is the main input. It consists of the incoming physical environmental information, represented by time series of ambient temperature, sun light radiation or infrastructure loads. Hence

this data is related to the actual operation area and application of the system. For this thesis an offline closed data set has been used, but for future applications it is extendable for the use of real-time data.

The next block is the system characterization, which is adapted for the specific application. The implementation has been designed for the loss prediction of the AIT Smart Grid-Converter (ASGC) inverter system, a device developed and produced by the Austrian Institute of Technology. In section 3.2 a detailed description of the system is given. Since all of our failure modules mainly base on component temperature, the system characterization contains in particular thermal models.

The simulation is universal and independent of the actual operation field and power electronic systems. It is the executive part of the implementation, based on the prepared parameters and information of the system characterization. The major wear-out cause of power electronics can be reduced to a set of components and their failure mechanisms. The focus in this thesis is on the electrolytic capacity and the IGBT semiconductor components, with their failure mechanisms described in Section 2. The incoming data series are divided into sections of time range Δt and the probability to failure is ongoing calculated for each time section. Originally starting with a fictive set of inverter systems and their components, a Monte Carlo Simulation (MCS) is used to evaluate the number of losses at each time step. This gives a step by step simulation and lifetime simulation.

The failure analysis of the loss results is represented with the last block of the flow diagram. Based on the outage time of components, a statistical analysis and lifetime prediction can be done. This block mustn't necessarily be a part of the implementation and could also be outsourced to another program.

3.1 Mission profile

The mission profile is a special term in robustness validation which is a representative physical dataset which drives fatigue of components, products or systems. It is a package containing parameters and time series of the application area and site. For example environmental influences which stress material like temperature profiles, mechanical vibrations, humidity, electric or magnetic fields.

The particular object of research for this thesis is the AIT ASGC inverter system. Therefore the mission profile contains physical, environmental information. It contains the ambient temperature, sun radiation as well as infrastructure load balance profiles. Since inverter systems are settled at a fixed site, it is defined to Vienna in Austria which is the location of the TU Wien and as well as the AIT. In the future the implementation may be extended to real-time applications but for this thesis offline data is used. A general issue in lifetime prediction and simulation is the opportunity to compare because fatigue occurs typically in ranges of years or decades. Mission profiles are not off-handedly available especially in a certain time resolution that is needed. Hence this fact information of a 2017 has been used and periodically composed for an never-ending series. This approach assumes that temperature courses are recurring and don not consider

irregularities or climate changes. In Figure 11 the ambient temperature and the sun radiation of the mission profile can be seen, extracted from measurements of the weather station[3] provided by the University of Natural Resources and Life Sciences, Vienna.

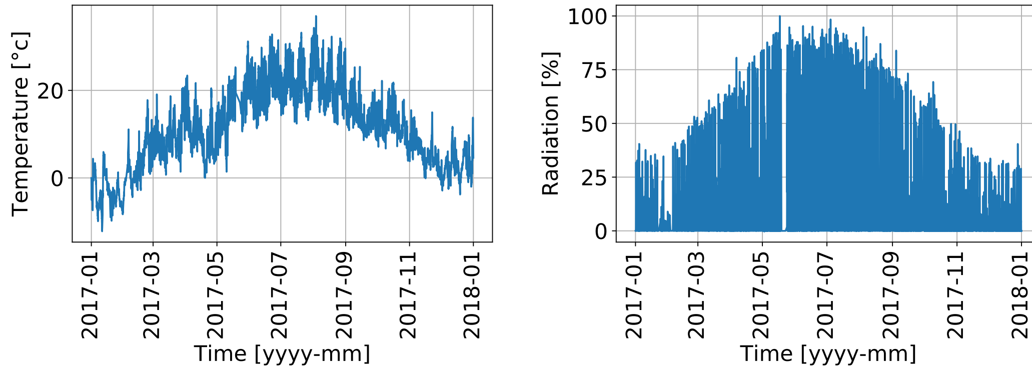

(a) Temperature course of one year. (b) Sun radiation in percent of one year.

Figure 11: Mission profile based on weather data of 2017 in Vienna, Austria.

For a more detailed illustration Figure 12 shows an extraction of one day of the mission profile with a resolution of 2.5 minutes. The original data had a resolution of 10 minutes but the data has been synchronised with the load profile by re-sampling and interpolation.

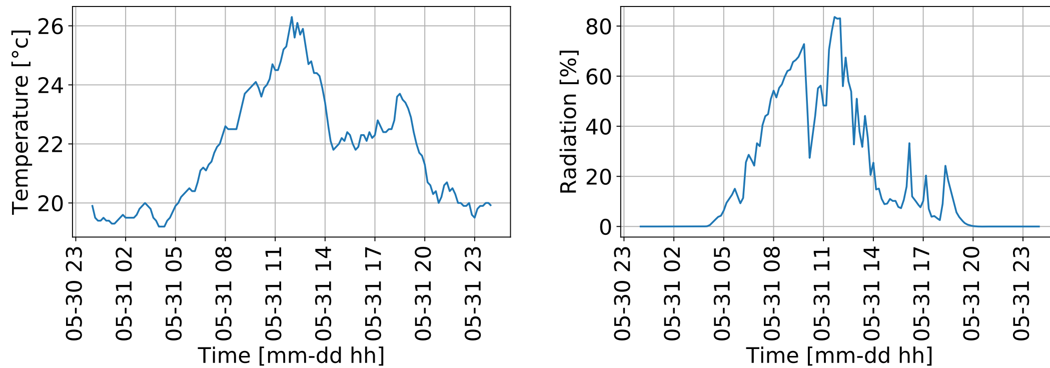

(a) Temperature course segment. (b) Sun radiation segment in percent.

Figure 12: Mission profile segment of one day.

The resolution limitation has special impact on the thermal swing detection, because cycles in between two data point are not available. More details to this subject will be discussed in Section 3.3 and Section 4.3 but it is always a compromise between data information and computation time. Beside the actual power

[3]https://meteo.boku.ac.at/wetter/mon-archiv/2017/201701/201701.html

supply driven by photovoltaic panels, the inverter system provides a compensation option for balancing asymmetric grid loads. More details will follow in Section 3.2. In order to represent a realistic scenario, the use of real infrastructure data was introduced. Thankfully low voltage load profiles were provided by Austrian Climate and Energy Fund (KLIEN) in the project "FACDS - Flexible AC Distribution Systems" (Project Number: 853555). For the further processing of the simulation and system characterization models actual current values are necessary. This balancing current $I_{balance}$ must be provided by the inverter system to balance the grid, regarding equal current amplitudes and symmetrical phase angles. The following conversion has been done by previous preparation and the time series and the balancing current $I_{balance}$ added to the mission profile as a load profile. In a future real-time scenario the computation probably has to be done in the implementation (e.g. the system characterization), depending on the availability of the provided inverter system informations. In the following, a short description is given how this process has been implemented. The goal of this pre-editing is to harmonize the phase angles and current amplitudes, starting with the load profiles

$$I_{load} = \begin{bmatrix} I_a \times e^{\phi_a} \\ I_b \times e^{\phi_b} \\ I_c \times e^{\phi_c} \end{bmatrix} \quad , \tag{3.1.1}$$

with different angles ϕ. The currents and phases depend on time, but for for reasons of clarity the index has been dropped and a certain time point considered. Next a current vector with equal phases is created by using the minimum of the angles

$$I_{equal\phi} = \begin{bmatrix} I_a \times e^{\phi_{min}} \\ I_b \times e^{\phi_{min}} \\ I_c \times e^{\phi_{min}} \end{bmatrix} \quad , \tag{3.1.2}$$

$$\phi_{min} = min(\phi_a, \phi_b, \phi_c) \quad . \tag{3.1.3}$$

Then resulting vector $I_{equal\phi}$ is transferred into zero, positive and negative sequence component system

$$I_{zpn} = M \times I_{equal\phi} \quad , \tag{3.1.4}$$

with the conversion matrix

$$M = \begin{bmatrix} 1 & 1 & 1 \\ 1 & e^{i\frac{2\pi}{3}} & e^{2i\frac{2\pi}{3}} \\ 1 & e^{2i\frac{2\pi}{3}} & e^{i\frac{2\pi}{3}} \end{bmatrix} \quad . \tag{3.1.5}$$

By removing the zero and negative, only the positive component with equal angles and amplitudes, which is the final balanced grid state.

$$I_{zpn} = \begin{bmatrix} I_z \\ I_p \\ I_n \end{bmatrix} \rightarrow I'_{zpn} = \begin{bmatrix} 0 \\ I_p \\ 0 \end{bmatrix} \quad . \tag{3.1.6}$$

Multiplying the inverse of the matrix M with I'_{zpn} re-transfers the current into the initial system. Forming the difference between the starting vector I_{load} and the result of the final balanced current $M^{-1} \times I'_{zpn}$ leads to the balance vector

$$I_{balance} = I_{load} - M^{-1} \times I'_{zpn} \quad , \tag{3.1.7}$$

which has to be provided by the inverter system to cancel the asymmetric components and ends up with a symmetrical and balanced grid.

For data protection reasons the load profiles cannot be shown here.

3.2 System characterization and modelling of the inverter system

The system characterization prepares data for the following simulation by the use of a system model. Fed with physical environment information and input parameters of component behaviour, the module generates data series. Regarding a selected set of components and failure modes of the system, their wear-outs are essentially driven by the component temperature. Therefore the primary purpose of the system characterization is to model the thermal behaviour of a certain power electronic system and represent the essential functionality. For this thesis the AIT Smart Grid-Converter (ASGC) inverter system has been studied, which has been developed and built by the AIT Austrian Institute of Technology. In the following an overview of the ASGC functionality is given and the characterization of the system. The analysis implies two individual thermal models for the IGBT semiconductors and the electrolytic capacitors, which also includes the thermal capacity of the inverter system.

3.2.1 AIT Smart Grid-Converter

Developing models and adopting the parameters requires expertise of the fundamental functionality as well as experience of the system and their components. For the characteristic parameters of the model a certain inverter has to be defined concerning its individual schematic and operation site. The collaboration with the AIT gives the opportunity to get insight of their technology and support of their yearlong experience on power electronic systems. The AIT Smart Grid-Converter (ASGC)[4] has been developed and produced by the AIT, therefore a detailed background knowledge of schematic, behaviour and functionality was available.

[4]https://www.ait.ac.at/themen/smart-grids/power-system-technologies-development-validation/ait-smart-grid-converter

Shortened to a sentence the ASGC is a DC-AC converter, converting supplied DC power for an AC consumer. It is a four phase, four wire converter for emerging Inertia Micro Grid applications. The focus is on converting supplied energy of photovoltaic systems to a low voltage grid. Additionally, the inverter system offers the possibility to balance the distribution network by the compensation of asymmetric loads in the grid. To protect the inverter of overstress, the system is limited to a maximum current or power, using a priority selection, either radiation conversion or grid balancing.
In the following paragraph the corner points of the data sheet are given.

Type	ASGC 34.5TL-EES-4P4W
DC max. input voltage	900V
DC max. PV/BATT operating current	60A
AC max. output power	34.5kW
AC max. continuous apparent power	34.5kVA
AC nominal output voltage	3 NPE 380V / 220V
AC operating voltage range	3 NPE 400V/230V +/-20%
AC nominal frequency	50Hz
AC Frequency range	45-55Hz
AC max. continuous output current	50A
Peak efficiency	98.7%
Weighted efficiency EU/CEC	98.2%

Features and capabilities

- Full four quadrant operation
- Active/Reactive power: full circular capability
- Immediate control: Conn, P, PF, Q, Volt-Var/Q(U)
- Frequency control: Frequency-Watt/P(f)
- Low/High Voltage ride through with Fast Reactive Current Response
- Primary frequency regulation
- Synthetic (virtual) inertia
- Grid forming and black start capability with unbalanced load conditions

The ASGC is using a NPC-2 inverter topology to convert the DC voltage into AC. Figure 13 shows a scheme of the inverter schematics.
On the left side of the schematics the DC-input voltage has to be provided by an external source (e.g. photovoltaic). The core parts are the four IGBT modules in the center of the scheme. They chop the constant DC-signal, ending up with a high frequency signal. The capacitor and inductor structure on the right part of the topology is filtering and smoothing the signal, ending up as an AC sine signal on the right output. The electrolytic capacitors (pooled to a collective

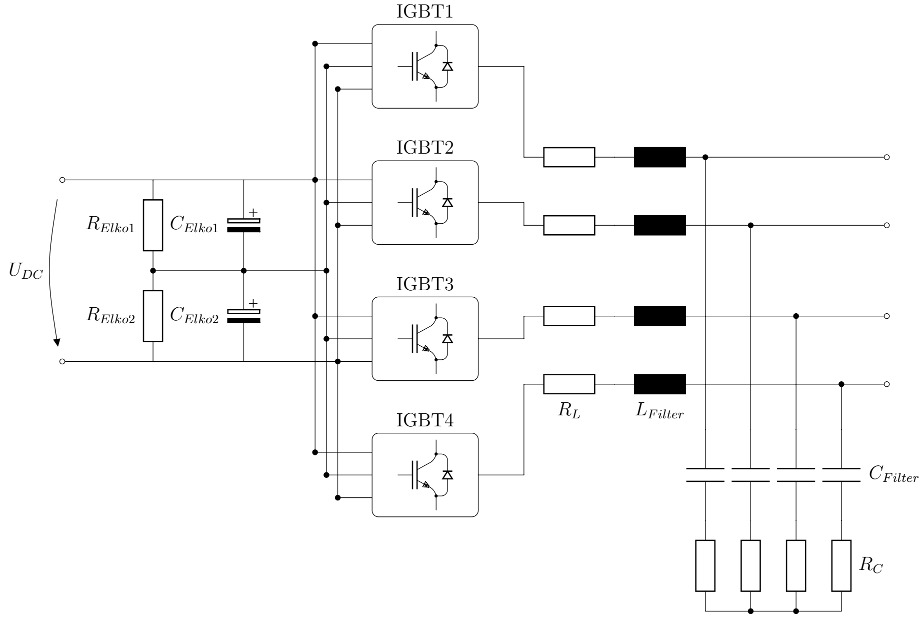

Figure 13: Scheme of the ASGC inverter's schematic.

symbols) next to the input buffer missing energy for the conversion. Figure 14 shows the top view of the ASGC with a removed covering panel. On the upper part of the image an capacitor array can be seen, these 24 electrolytic capacitors are pooled together for the schematics into two symbols in Figure 13. Since the IGBT module is working with a high switching frequency to chop the signal, the electrolytic capacitors have to provide the power with the same sample rate. This fact is incorporated into the calculation for the power loss of the capacitors and essential for the electrolytic capacitor failures.

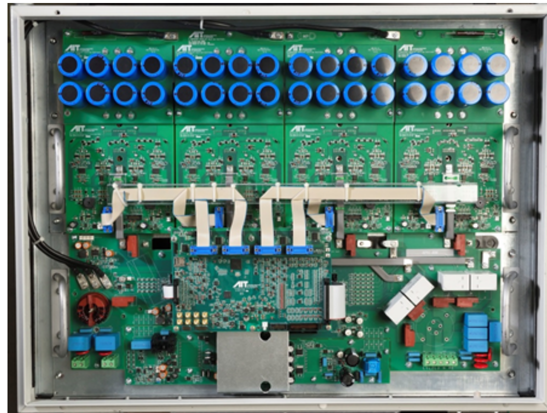

Figure 14: Top view of the ASGC without covering panel.

3.2.2 Measurement for system characterization

Since all discussed failure mechanisms are primary driven by temperature, the thermal behaviour of the system and therefore the relations between power performance,

ambient temperature and the resulting component temperature are essential. Thermal measurement results of the system leads to a derivation of the fundamental thermal model structure. In the following section the experimental setup, the measurement results and the consequences for the model structure will be discussed.

The characteristics of the system are determined by a performance test, beginning with a cold start and following with an immediate rise to full load. The whole system is therefore starting at homogeneous temperature, in equilibrium with the ambient. In order to simulate a realistic application, the inverter system is connected to a virtual grid environment. With the rising load, the power loss and hence the temperature are both increasing continuously till a steady-state has been reached. The temperature distribution may be inhomogeneous, depending on the disposal of the component and position of the cooling system.

Experimental setup The experimental setup is adjusted with various monitoring points which gives us the possibility to get knowledge of the temperature distribution of the system and therefore to derive a thermal model. In Figure 15 a picture of the layout and experimental setup of the system is given.

Figure 15: Setup of thermo-couples and air ventilation.

At the top of the image an array of electrolytic capacitors can be seen. The entire array can be segmented into three sets, corresponding to the separate phases of the inverter. In order to evaluate the temperature distribution and variances between the electrolytic capacitors array, a set of type J thermocouple(Fe-CuNi) measuring elements have been assembled at outer and inner positions. Figure 16 shows a schematic of the array, the segmentation into the three phases and the six thermocouple positions. The measurement points are labelled with the mask: $Sub\,\mathbf{W}_P\,\mathbf{X}\,C\,\mathbf{Y}\,\mathbf{Z}$ and the keys of Table 1.

The IGBT switching elements are embedded under covering panels and therefore not visible at Figure 15. They are positioned in the center of the layout

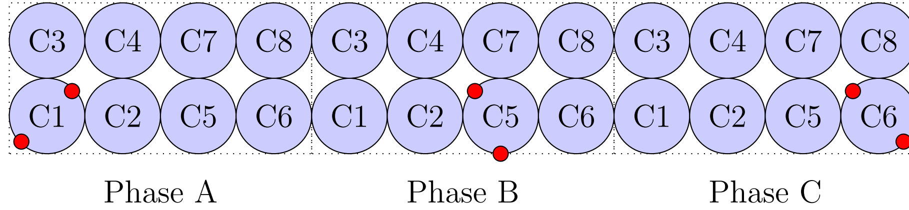

Figure 16: Displacement of measuring elements at electrolytic capacitor array.

W	Pin number of measurement board
X	Phase (A,B or C)
Y	Number of the capacitor (1,2,...,8)
Z	Position (inside(I),outside(A))

Table 1: Keys of legend label mask $Sub\,\mathbf{W}_P\,\mathbf{X}\,C\,\mathbf{Y}\,\mathbf{Z}$.

and assembled with type K thermocouples(NiCr-Ni) measuring elements. The ventilation system is positioned on the left side of the image below the IGBTs circulating the air clockwise.

Measurement procedure The performed characterization test is starting in at initial state with no power consumption and the system in equilibrium with the ambient and hence homogeneous temperature distribution (depending on the location). At the beginning of the measurement, the system will be stressed by an immediate rise of the load from zero to the approved maximum. The power loss causes heat production and an increasing temperature. The following thermal dynamics in the system can be interpreted as a step response of the system. The increasing temperature will then be in-homogeneously distributed over the layout design and their integrated components. Goal of this setup is to analyse the temperature rise together with the temperature distribution and variation between the electrolytic capacitors as well as for the IGBTs. With the measurement results, approaches for the thermal model can be made. In particular the thermal capacity of the system is of interest and the analysis of the time lag of component temperature related to a changing of power loss and ambient temperature. The measurement software only supports an unitary adjustment for one thermocouple type. The different types of the used thermocouples raise the problem that only capacitors or IGBT can be recorded correctly and caused by the distinguished types, a conversion is required. With the knowledge of previous measurements, the capacitors indicate a more extraordinary temperature behaviour, therefore the adjustment has been set to type J.

Measurement results The experiment has been finished after a runtime of 3.5 hours, when the system seemed to have reached a steady state. In the following, the results of the step response performance test will be shown. Starting with the electrolytic capacitors, some interesting results regarding the thermal capacity of the system can be derived, thereafter the IGBT measurement will be discussed

and interpreted.

The component temperature curves of the electrolytic capacitors in Figure 17 show a slowly increasing course.

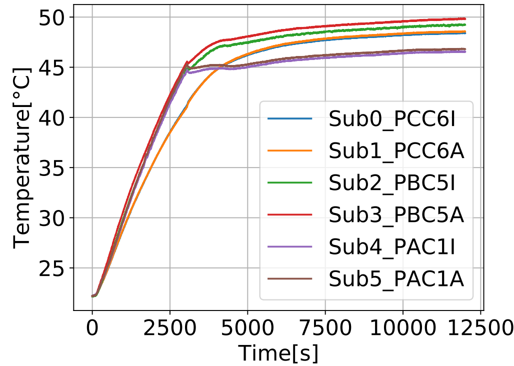

Figure 17: Measurement of capacitor temperatures at different positions of the layout. When reaching a temperature limit at the system, the ventilation starts cooling. Caused by the displacement of ventilator and capacitor array, this is not entire homogeneous.

At the beginning all component temperatures are approximately equal until the ventilation system starts cooling the system. A sudden change of the capacitors in phase A, which are closest to the ventilation, can be detected at the reach of 45 °C. In the following the deviation of the other temperature curves also change and they converge to a steady state after about 2 hours. This slowly increasing and delayed rise of the temperature can be interpreted as a thermal capacity of the system. Therefore this behaviour is not limited to a temperature rise and one can assume the delay to also occur for a decreasing temperature. Looking at the differences of amplitudes, the spread between the temperatures is small. Hence this fact, in the first instance an unitary thermal model is suitable.
Figure 18 visualises the converted IGBT temperature behaviour, recorded according to another thermocouple type.

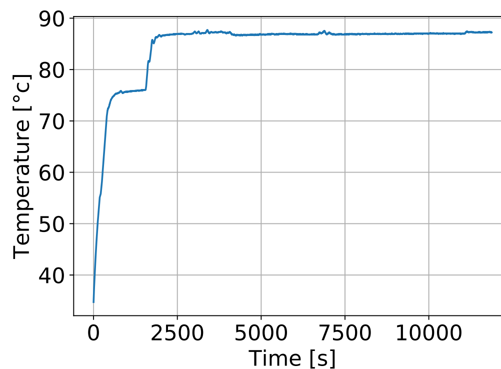

Figure 18: Measurement of IGBT phase two temperature.

The thermocouple types of the IGBT and the capacitors are different and the relation is defined in a conversion table[5]. Nevertheless the results show a much faster rise of the IGBT temperature in comparison to the capacitors. Therefore no thermal capacity has been considered for the IGBTs. Limited in measurement slots, only one IGBT has been recorded. But since the loads are nearly equal balanced to all phases it can be assumed that all IGBTs behave the same. This assumption is also established by previous measurements. Figure 19 shows the screenshot of the monitoring program at the steady state with real-time values of (another) measurement entity. In particular the IGBT currents and the corresponding component temperatures are of interest and relevant for the thermal models.

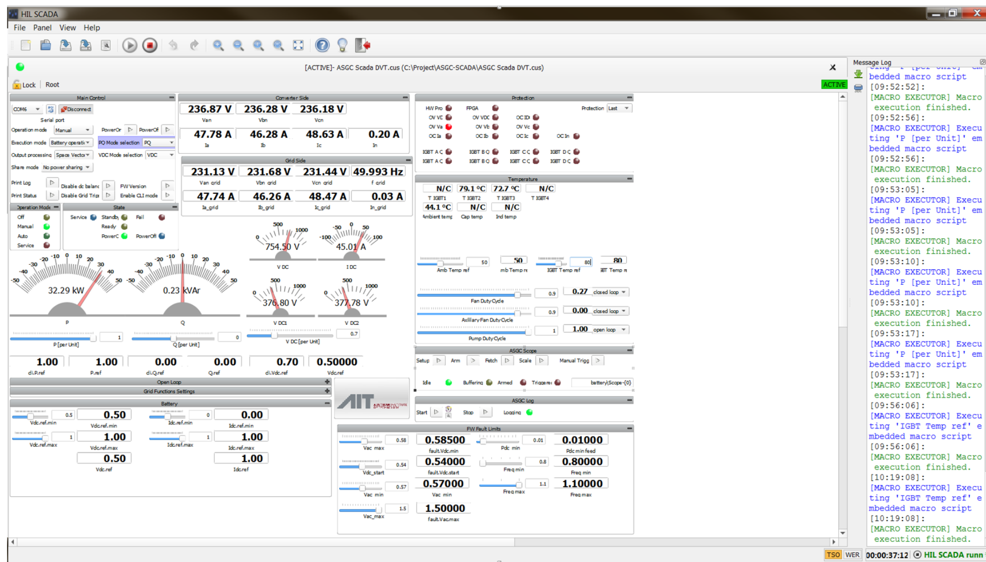

Figure 19: Screenshot of the program settings and actual measurements.

The analysis was limited in experimental and laboratory operation time. For future works additional results should yield more advanced and precise models.

3.2.3 Thermal model of the electrolytic capacitors

The heating of electrolytic capacitors is driven by two parameters: the ambient temperature and the power loss. To formulate the thermal model, the system has been divided into several thermal stages and junctions. Figure 20 shows a scheme of the model structure and the junctions. In general, every inner space is always influenced by outer temperature, plus heat production in this area. Hence this consideration, the model is starting with the ambient temperature at the outside of the system and continuously adding junction temperature. The first junction leads the ambient to the inside of the system, then to the component surface and finally to the core.

[5] https://srdata.nist.gov/its90/menu/menu.html

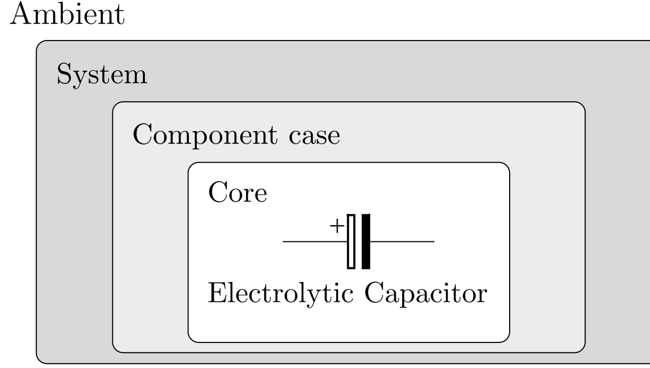

Figure 20: Scheme of the sections for the electrolytic capacitor thermal model.

Ripple current Before formulating the actual model, a declaration of the current and the composition of the ripple is given which effects the power loss and therefore the heat production. Starting with the essential input factors, the sun radiation is given by the mission profile of Section 3.1 corresponding to the application. The sun radiation supplies power and a resulting electric current

$$P_{radiation} = P_{max} \times Radiation\,[\%] \quad , \tag{3.2.1}$$

$$I_{radiation} = \frac{P_{radiation}}{230\,\mathrm{V}} \quad , \tag{3.2.2}$$

with $P_{max} = 230\,\mathrm{V} \times 50\,\mathrm{A} = 11\,500\,\mathrm{W}$ as the maximum power for each phase of the inverter.

Another input is the balancing current $I_{balance}$ time series of a certain distribution network due to compensate asymmetric grid loads. The balancing current together with the radiation current $I_{radiation}$ sum up to a total current. Nevertheless this could result in a total current larger than the limit. Therefore the build-in function I_{option} limits the current to $I_{max} = 50\,\mathrm{A}$ and furthermore offers a priority setting of radiation conversion or grid balancing.

$$I_{total} = function\,\mathbf{I_{option}}(\boxed{I_{radiation}}, \boxed{I_{balance}}, \boxed{\text{"}option\text{"}}) \quad . \tag{3.2.3}$$

In Table 2 an explanation is given for I_{option} function options.

Figure 21 shows a visualised example for the *prioritysym* option to prioritize balancing before converting the radiation.

Caused by the overgrown sum of $I_{radiation}$ and $I_{balance}$, the current vector has been reduced by the multiplication factor α, so that the absolute vector $abs(I_{balance} + \alpha \times I_{radiation})$ is not larger than $I_{max} = 50\,\mathrm{A}$. The total current I_{total} must not be symmetrical with a component shift of $\frac{2\pi}{3}$rad, due to asymmetric balancing load parts. The heat production is caused by two impact factors, both related to the total current I_{total}. Firstly the heat production of the system due to power loss is caused by the absolute amplitude of the current vectors, independent of the phases. Secondly the composed ripple current is essential for the

option	description
prioritysym	Priority for the $I_{balance}$. If the absolute vector of the sum $I_{radiation} + I_{balance}$ is larger than $I_{max} = 50\,\text{A}$, only the fit part of $I_{radiation}$ will be added.
onlysym	Only $I_{balance}$; $I_{radiation}$ will not be added.
priorityrad	Priority for the $I_{radiation}$. If the absolute vector of the sum $I_{radiation} + I_{balance}$ is larger than $I_{max} = 50\,\text{A}$, only the fit part of $I_{balance}$ will be added.
onlyrad	Only $I_{radiation}$; $I_{balance}$ will not be added.

Table 2: Options and description of function I_{option}.

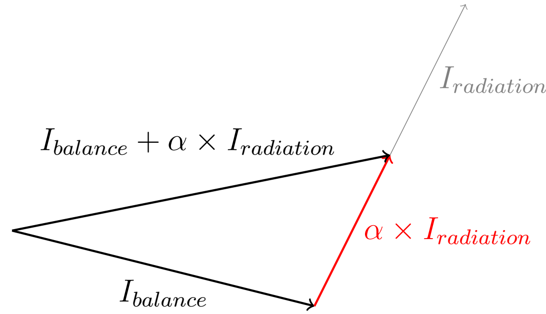

Figure 21: Example for I_{option} with *priorityrad* and there priority for $I_{balance}$.

warming of the capacitor itself. The ripple current is formed by the superposition of the current components. Figure 22 shows two examples and a comparison of how the component shift can affect the sum.

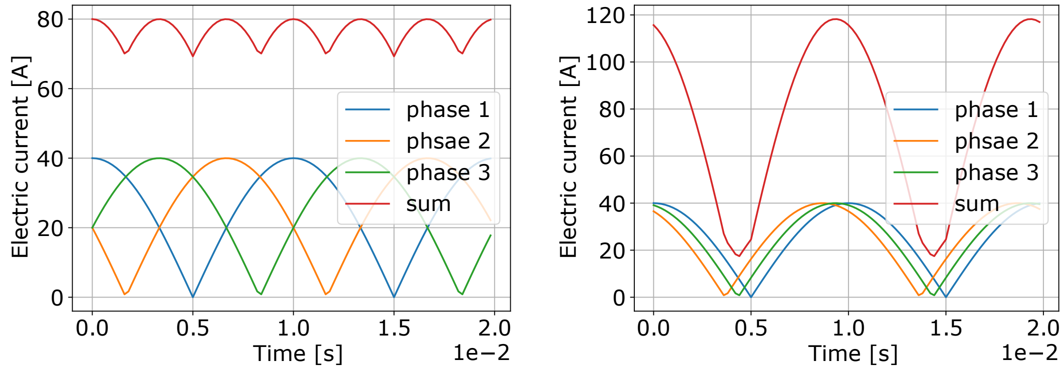

(a) phase shift of $\frac{2\pi}{3}$rad.

(b) phase shift close to zero.

Figure 22: Examples of ripple signal, caused by different phase shifts.

The signal form is reasonable for its name "ripple". Figure 22a shows a signal of a symmetric components with equal phase differences of $\frac{2\pi}{3}$rad. The gap between the maximum and minimum of the ripple signal is small compared to Figure 22b. The three components are nearly in phase which results in a sum signal

Frequency (f)	Multiplication factor (MF)
$f \leq 50\,\mathrm{Hz}$	0.90
$50\,\mathrm{Hz} \leq f < 100Hz$	0.95
$100\,\mathrm{Hz} \leq f < 120\,\mathrm{Hz}$	1.00
$120\,\mathrm{Hz} \leq f < 200\,\mathrm{Hz}$	1.15
$200\,\mathrm{Hz} \leq f < 1000\,\mathrm{Hz}$	1.30
$1000\,\mathrm{Hz} \leq f$	1.40

Table 3: Frequency ranges and corresponding multiplication factors.

with higher amplitude but lower frequency. The reason why the sine-component signals are only positive is that the IGBTs (see Figure 13) changes the current direction for the output at every half period. This means that on the input side where the electrolytic capacitors are positioned, the phase signal occurs like in Figure 22 and on the output side there are full AC sine signals with positive and negative values. After forming the superposition, the signal is separated into its frequency components using a Fast Fourier Transformation (FFT). For the further computation the frequency components are classified into ranges which are given in Table 3. The ripple current can be calculated by the sum of squares of the current components and their corresponding multiplication factors

$$I_{ripple} = \sqrt{\sum_i ((MF)_i \times I_i)^2} \quad , \tag{3.2.4}$$

where I_i are all current parts in a certain range.

Thermal model After the current declaration and the composition of the resulting ripple signal, the next section discusses the formulation of the thermal model for the electrolytic capacitors. First of all, the essence of Figure 20 must be transferred into a mathematical formulations. Therefore the capacitor's core temperature, which is the innermost part of the model, has been composite with the outermost temperature and several sequential added temperature junction gaps.

$$T^{cap}_{core} = T_{ambient} + \Delta T^{cap}_{system} + \Delta T^{cap}_{surface} + \Delta T^{cap}_{core} \quad . \tag{3.2.5}$$

Heat production is caused by a power loss due to flow of electricity. Considering the layout design, the ripple current is the essential factor affecting the temperature rise. An approximation for $\Delta T^{cap}_{surface}$ and ΔT^{cap}_{core} has already been given in the theoretical description in Section 2.2 by Equation 2.2.6:

$$\Delta T^{cap}_{surface} = \frac{I^2_{ripple} \times R_{ESR}}{\beta_e \times A} \quad , \tag{3.2.6}$$

$$\Delta T^{cap}_{core} = \frac{1}{\alpha} \times \Delta T^{cap}_{surface} \quad . \tag{3.2.7}$$

Considering the electrolytic capacitor with capacitance $C = 470\,\mathrm{uF}$ and $D = 3.5\,\mathrm{cm}$, $L = 5\,\mathrm{cm}$ [8], the parameters have been defined by

$$
\begin{aligned}
A &= D\pi \times L + \frac{D^2\pi}{2} = 64.60\,\mathrm{cm}^2 \quad , && && (3.2.8)\\
R_{ESR} &= 0.45\,\Omega \quad , && [8] && (3.2.9)\\
\beta_e &= 1.66 \times 10^{-3}\,\mathrm{W/cm}^2 \quad , && [32] && (3.2.10)\\
\alpha &= 0.64 \quad . && [32] && (3.2.11)
\end{aligned}
$$

$T_{ambient}$ can be extracted and I_{ripple} computed from the mission profile. Therefore the only unknown term is ΔT^{cap}_{system}. For an approximation, the result of the system characterization (shown in Figure 17) will be considered in the following. Since all measurement results are close to each other and the differences of temperature amplitudes are small, an ordinary approach has been made by using the "worst-case" scenario and an unitary model for the entire set of capacitors. Meaning that the highest temperature course is used for the representation of the whole electrolytic capacitor array.

The temperature difference between the measurement start and the final temperature results

$$
T^{cap}_{surface}(t_{final}) - T^{cap}_{surface}(t_{start}) \approx 30\,^\circ\mathrm{C} \quad . \tag{3.2.12}
$$

Using

$$
T^{cap}_{surface}(t) = T_{ambient}(t) + \Delta T^{cap}_{system}(t) + \Delta T^{cap}_{surface}(t) \tag{3.2.13}
$$

yields

$$
\begin{aligned}
T^{cap}_{surface}(t_{final}) - T^{cap}_{surface}(t_{start}) &= \Delta T^{cap}_{system}(t_{final}) - \Delta T^{cap}_{system}(t_{start}) && (3.2.14)\\
&+ \Delta T^{cap}_{surface}(t_{final}) - \Delta T^{cap}_{surface}(t_{start}) \quad , && (3.2.15)
\end{aligned}
$$

by considering constant ambient conditions $T_{ambient}(t_{start}) = T_{ambient}(t_{final})$.

The measurements have been made in the AIT laboratories under virtual grid conditions. With the assumption of a symmetrical grid and therefore angle variances smaller than 10°, the difference

$$
\Delta T^{cap}_{surface}(t_{final}) - \Delta T^{cap}_{surface}(t_{start}) \leq 1^\circ \tag{3.2.16}
$$

can be neglected. Hence this approximation the derivation ends-up with

$$
\Delta T^{cap}_{system}(t_{final}) - \Delta T^{cap}_{system}(t_{start}) \approx 30\,^\circ\mathrm{C} \quad . \tag{3.2.17}
$$

This temperature gaps exists for the maximum load. For a general approach, the temperature relation has been considered as linear with means of the absolute current vectors

$$\Delta T_{system}^{cap} = \frac{mean(abs(I_{total}))}{I_{max}} \times 30\,°\mathrm{C} \quad . \tag{3.2.18}$$

After approximating all terms of the thermal model, for a complete approach the thermal capacity has to be considered as well. Again, the "worst-case" will be assumed and the highest temperature course used for a the model fit. In Figure 23 the normalized temperature curve has been plotted and a fit done.

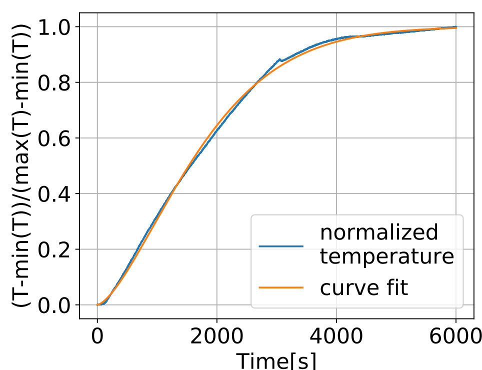

Figure 23: Normalized temperature course and fit curve, interpreted as the thermal capacity of the system.

For the fit the formula

$$T_{fit}^{cap} = 1 - e^{-\frac{t^a}{\tau}} \quad , \tag{3.2.19}$$

$$\tag{3.2.20}$$

has been applied and parameters

$$\tau = 82081s \quad , \tag{3.2.21}$$

$$a = 1.493 \quad . \tag{3.2.22}$$

have been computed. As a consequence of the thermal capacity, every temperature change will be delayed with an exponential in- or decrease. In order to get a sense for the change of temperature, Figure 24 shows the distinction when applying the thermal capacity.

For an individual model for each position of the capacity array, measurement curves for different current loads have to be done in future works. To give an outlook, a bigger set of measurement points would also enable a validation of the linear approach for T_{system}^{cap} and the exponential decrease assumption.

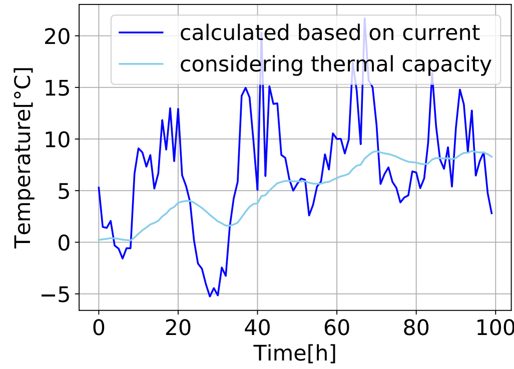

Figure 24: Comparison of capacitor temperature by considering the thermal capacity of the system. Particularly the impact of temperature fluctuations and peaks is reduced.

3.2.4 Thermal model of the semiconductors

The heating of the IGBT semiconductors is driven by the ambient temperature and the power loss. This identity is equally to the electrolytic capacitors. But in distinction, here the total current I_{total} is the only influencial factor and it is independend of the ripple (due to the schematic). For the theoretical formulation the well establish Cauer model is used to characterize the thermal behavior. The Cauer model describes the heat transformation between different layers and materials (in an IGBT) with a thermal circuit model by dividing it in several R- and C-terms. The Cauer model as well as the coexisting Foster model is often used to describe the internal heat flow of a semiconductor, beginning at the case surface of the module. In contrast to the Foster model, each layer and node of the Cauer model has a physical representation of the internal behavior. This means that the analogon of a voltage in an electrical circuit is a certain temperature at a layer model. [16] To approximate the case temperature, the internal thermal model has to be extended until the boundary of the system, the ambient. For the previous model of the electrolytic capacitors the fundamental concept of the Cauer model has already been used but not termed because the specific exponent of the thermal capacity could not be represented using this theory. Concluded by the system characterization measurements, no capacity has been assumed and the junction temperature is therefore given by series circuit of thermal resistances. In Figure 25 the schematics of the Cauer model for the semiconductor is shown.

The schematic is straightforward consisting of two thermal resistances between the ambient and the junction and no capacity. Moreover a more detailed model would be possible in future works by increasing the quantity of system characterization measurements and measurement points. The relevant component temperature for failure modes is the operation temperature or junction temperature T_{vj}^{semi}. Combining the case-to-junction resistances R_{ctj}^{semi} and ambient-to-case resistances R_{atc}^{semi} to the thermal resistance

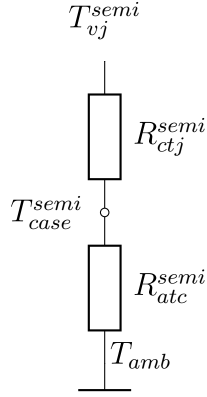

Figure 25: Junction Temperature T_{vj}^{semi} evaluated using the Cauer model.

$$R_{th}^{semi} = R_{ctj}^{semi} + R_{atc}^{semi} \quad , \tag{3.2.23}$$

allows the junction temperature T_{vj}^{semi} to be formulated by using the ambient temperature and the power loss

$$\begin{aligned} T_{vj}^{semi} &= T_{amb} + P_{loss} \times R_{th}^{semi} && (3.2.24)\\ &= T_{amb} + P_{loss} \times (R_{atc}^{semi} + R_{atj}^{semi}) && (3.2.25)\\ &= T_{case}^{semi} + P_{loss} \times R_{ctj}^{semi} \quad , && (3.2.26)\\ T_{case}^{semi} &= T_{amb} + P_{loss} \times R_{atc}^{semi} \quad . && (3.2.27) \end{aligned}$$

The IGBT internal thermal resistance

$$R_{ctj}^{semi} = 0.2\,\frac{\mathrm{K}}{\mathrm{W}} \qquad [17] \tag{3.2.28}$$

is specified in the datasheet.

R_{atc}^{semi} is the unknown variable but can be deviated by the temperature difference between the ambient and the IGBT surface temperature. Therefore Equation 3.2.26 will be solved with the measurement results of Section 3.2.2 and after then R_{atc}^{semi} can be computed by inserting into Equation 3.2.27. The most reasonable results of the system characterization measurements are extracted and inserted in Table 4.

Caused by the failure of the measurement unit of the first IGBT, this row and its values have not been inserted. Last row shows the mean values of currents and temperatures.

The power loss P_{loss} composites of a switching loss and the electric power of the IGBT

	Total current I_{total}[A]	Case temperature T_{case}^{semi}[°C]
IGBT 2	46.26	80.0
IGBT 3	48.47	72.4
mean	**47.37**	**76.2**

Table 4: Steady state values of the inverter system characterization with the maximum load applied.

$$P_{loss} = P_{switch} + P_{elec} \quad , \tag{3.2.29}$$

$$P_{switch} = (E_{on} + E_{off}) \times f = (2.0 + 5.3)\text{mJ} \times 20\,\text{kHz} = 146.0\,\text{W} \quad , \tag{3.2.30}$$

$$P_{elec} = I_{case(mean)} \times V_{CESAT} = 47.37\,\text{A} \times 1.6\,\text{V} = 75.8\,\text{W} \quad , \tag{3.2.31}$$

with

$$E_{on} = 2.0\,\text{mJ} \quad , \qquad [17] \tag{3.2.32a}$$

$$E_{off} = 5.3\,\text{mJ} \quad , \qquad [17] \tag{3.2.32b}$$

$$V_{CESAT} = 1.6\,\text{V} \qquad [17] \quad . \tag{3.2.32c}$$

for an approximative $T_{vj}^{semi} = 125\,°\text{C}$.

Therefore the junction temperature is given by

$$T_{vj}^{semi} = T_{case}^{semi} + P_{loss} \times R_{ctj}^{semi} = 76.2\,°\text{C} + 44.4\,°\text{C} = 120.6\,°\text{C} \quad , \tag{3.2.33}$$

$$P_{loss} \times R_{ctj}^{semi} = (146\,W + 75.8\,W) \times 0.2\,\frac{\text{K}}{\text{W}} = 44.4\,\text{K} \quad . \tag{3.2.34}$$

Despite the increasing internal system temperature, the environment stays constant with an ambient temperature $T_{amb} = 22.2\,°\text{C}$. Insert this in Equation 3.2.27 yields

$$P_{loss} \times R_{atc}^{semi} = T_{case}^{semi} - T_{amb} = 76.2\,°\text{C} + 22.2\,°\text{C} = 54.0\,°\text{C} \quad . \tag{3.2.35}$$

$$R_{atc}^{semi} = \frac{T_{case}^{semi} - T_{amb}}{P_{loss}} = \frac{54.0\,°\text{C}}{221.8\,\text{W}} \tag{3.2.36}$$

$$\rightarrow R_{atc}^{semi} = 0.24\,\frac{\text{K}}{\text{W}} \tag{3.2.37}$$

This deviation for the thermal resistance between ambient and case is the last piece for the thermal model of the semiconductor in Equation 3.2.24 with

$$R_{th}^{semi} = R_{atc}^{semi} + R_{ctj}^{semi} = (0.24 + 0.2)\frac{\text{K}}{\text{W}} = 0.44\,\frac{\text{K}}{\text{W}} \quad . \tag{3.2.38}$$

3.3 Modules and simulation

After introducing the system characterization and therefore the parameters and time series that drive the ageing, this section contains the description of the failure models and the actual lifetime simulation. These modules and in particular the failure processes are independent of the application field and inverter system. Therefore it can be applied to any power electronic system. In Figure 26 the essential block of the overview of Figure 10 is shown.

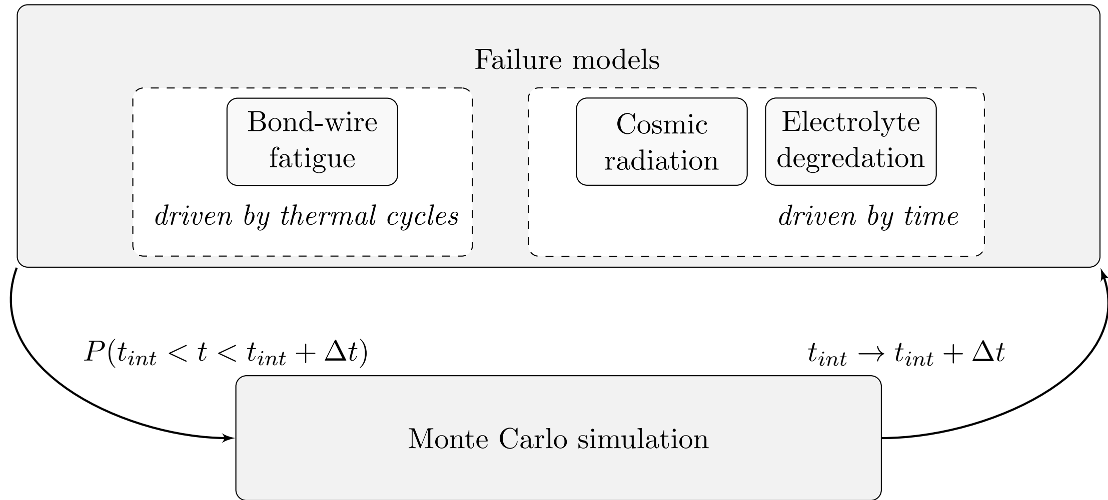

Figure 26: Simulation flow chart.

In this thesis there is a distinction between simulation of ageing processes in time and thermal cycles. Therefore, in the flow diagram the failure models are divided into separate blocks. In fact, these variants are not completely different and independent of each other because the thermal cycles are also related to a time course (which gives us the connection to combine them in a mutual analysis afterwards), but the simulations are running in different bases. The simulation procedure is starting by splitting the information of the system characterization into equal time sections Δt. This is especially useful for the identification of thermal cycles but also reduces the number of execution steps and therefore limits computation time. The time sections (resolution) are adjustable and as already mentioned maintain the relation of thermal cycles and time. In a real-time scenario the splitting of time series is also meaningful with equal scheduled waiting periods for the next execution step. Initially, a set of (virtual) functional systems is provided for the lifetime simulation. These systems contain several different components and failure mechanisms. The simulation is an iterative process, alternating between failure probability computation and losses prediction. The probability of a component failure results of the calculation for the current time section together with the previous probability, which considers the history of the ageing process. By using a Monte Carlo random experiment the simulation computes the number of fatiguing components in a (shrinking) set of (available) systems. This execution loop provides a step by step simulation and is running until all systems have failed or a certain simulation time has reached.

In the following a detailed failure model description of the ageing and fatigue processes is given. The theoretical background of these power electronics weak spots are discussed in Section 2.

3.3.1 Modelling of fatigue processes based on time course

Time is not in all cases the absolute parameter for ageing processes but intrinsic, physical environment factors (e.g. temperature, humidity, vibrations, electrical stress) are primarily responsible and change by the course of time. Meaning that the influencing factors as well as the the simulation are related to the progress in time. In the following, the two fatigue processes will be considered: degradation of electrolytic capacitors and failures caused by cosmic radiation.

Electrolytic capacitor degradation The degradation process of electrolytic capacitors is affected by several parameters. The most important one is the temperature, followed by the voltage. Equation 2.2.19 describes the lifetime estimation. Since the operation voltage is constant, the capacitor core temperature T_{core}^{cap} is the relevant fluctuating factor and only variable. Therefore the lifetime estimation model has been reduced to the form

$$L_x(t) = L_0 \times f_T(T_{max} - T_{core}^{cap}(t)) \times f_V(V_O) \quad , \tag{3.3.1}$$

$$f_T(T_{core}^{cap}) = e^{\frac{E_A}{k_B}(\frac{1}{T_{core}^{cap}(t)} - \frac{1}{T_{max}})} \quad , \tag{3.3.2}$$

$$f_V(V_O) = f_V = (\frac{V_R}{V_O})^7 = constant \quad . \tag{3.3.3}$$

with constants and parameters

$$\text{Boltzmann constant } k_B = 8.62 \times 10^{-5}\,\text{eV}\,\text{K}^{-1} \quad , \tag{3.3.4}$$

$$\text{Operating voltage } V_O = 450\,\text{V} \quad , \tag{3.3.5}$$

$$\text{Activation energy } E_A = 0.94\,\text{eV} \quad , \quad [35] \tag{3.3.6}$$

$$\text{Maximum rated temperature } T_{max} = 378.15\,\text{K} \quad , \quad [8] \tag{3.3.7}$$

$$\text{Maximum rated voltage } E_r = 500\,\text{V} \quad , \quad [8] \tag{3.3.8}$$

$$\text{Useful life } L_0 = 6000\,\text{h} \quad , \quad [8] \tag{3.3.9}$$

determined by the attached citations.

It must be distinguished between the simulation time t which references to the physical parameters (like the temperature) and the distribution time $\bar{t}$. At the beginning of the simulation both times start at zero $t = 0$ and $\bar{t} = 0$. A new iteration step usually comes together with a new core temperature $T_{core}^{cap}(t)$ at the beginning of the time section Δt. The two parameters β_e and η_e of the Weibull distribution are essential for the calculation of the failure probability. Considering reference [35], it has been assumed that

$$\eta_e(t) := L_x(t) \quad , \tag{3.3.10}$$
$$\beta_e = 7 \quad . \tag{3.3.11}$$

Therefore the scale parameter or characteristic lifetime $\eta_e(t)$ depends on the time t and therefore the core temperature $T^{cap}_{core}(t)$. For the calculation of the failure probability, the Weibull distribution has been used. According to Equation 2.1.5 the failure rate for the electrolytic capacitor is given by

$$h_e(\bar{t}) = \eta_e^{-\beta_e} \times \beta_e \times \bar{t}^{\beta_e - 1} \quad . \tag{3.3.12}$$

A changing core temperature $T^{cap}_{core}(t)$ leads to a new $\eta_e(T^{cap}_{core}(t))$. Therefore, the distribution time $\bar{t}$ has to be re-calculated for the previous time step $\bar{t} - \Delta t$ with the new $\eta_e(T^{cap}_{core}(t))$

$$\bar{t}(\eta_e(t)) = \left(\frac{h_e(\bar{t} - \Delta t)}{\eta_e^{-\beta_e}(t) \times \beta_e}\right)^{\frac{1}{\beta_e - 1}} \quad , \tag{3.3.13}$$

and hence this leads the the actual the failure rate

$$h_e(\bar{t}) = \eta_e^{-\beta_e}(t) \times \beta_e \times (\bar{t} + \Delta t)^{\beta_e - 1} \quad . \tag{3.3.14}$$

Semiconductor cosmic radiation failures The failure caused by cosmic radiation was discovered in the 1990's and affects all power electronic semiconductor devices like diodes, thyristors, GTOs, IGCTs, IGBTs, etc. [3] In contrast to the degradation effect, this failure mechanism is not an ageing process and yields in a constant failure rate at steady parameters. The failure probability is affected by high current or voltage and depends on component and environment parameters. The semiconductor failure is on one hand driven by the junction temperature T^{semi}_{vj} and distribution voltage V_{DC} and on the other hand depend on the intensity of the cosmic radiation. The amplitude of the radiation is particular related to the altitude above the sea-level *height* of the operation field. It is also varying on meridian and latitude of the earth which has not been considered in this thesis. It is a well-known effect and especially studied by many power electronic manufacturers. The model for this theses has been composed of three functions. The failure rate h_c for the cosmic radiation can be separated into

$$h_c(T^{semi}_{vj}, height, V_{DC}) = f_T(T^{semi}_{vj}) \times f_h(height) \times f_V(V_{DC}) \quad . \tag{3.3.15}$$

Two of these functions have been developed by [3]:

$$f_T(T_{vj}^{semi}) = \exp(\frac{298.15\,\text{K} - T_{vj}^{semi}}{47.6\,\text{K}}) \quad , \tag{3.3.16}$$

$$f_h(height) = \exp(\frac{1 - (1 - \frac{height}{44300})^{5.26}}{0.143}) \quad , \tag{3.3.17}$$

with junction temperature T_{vj}^{semi} in K and sea-level *height* in m.

The voltage model of [3] is not compatible with the manufacturer test results. Therefore, the $f_V(V_{DC})$ function has been derived of a fit process of the manufacturers application note.

$$f_V(V_{DC}) = a \times \exp(b \times V_{DC}) \quad , \tag{3.3.18}$$

with the fit parameters

$$a = 1.754 \times 10^{-2}\,\text{FIT} \quad , \tag{3.3.19}$$

$$b = 3.3 \times 10^{-2}\,\text{V}^{-1} \quad . \tag{3.3.20}$$

FIT is the number of failures within 10^9 element hours.

3.3.2 Modelling of fatigue processes based on thermal cycles

The challenge of fatigue processes which are not (primary) driven by time is to convert the information into another basis, run the simulation but still keep the relation between the new and old basis for a shared analysis. The fatigue process that is discussed here is the bond-wire degradation which is driven by thermal swings.

In Section 3.3.1 another outage model caused by cosmic radiation has been discussed, which is also not primarily driven by time because the failure rate remains constant when the parameters are steady. But the essential distinction is the basis of the simulation, which is the course of time for the cosmic radiation failure and thermal cycles for the bond-wire degradation.

To deal with the fact that this mechanisms as well as the simulation base on thermal cycles instead of time, a conversion method is applied. In this work the well established rainflow algorithm is used as a counter cycling method. The rainflow algorithm counts thermal cycles in a given time section and therefore reduces the complex time series into a set of two-tuple, composite the temperature gaps and their number of cycles. The scheme of the whole execution process is visualized in Figure 27.

The input is a time series of the junction temperature T_{vj}^{semi} provided by the thermal model applied to the mission profile. The temperature course is then separated in equal time sections Δt (simulation step sizes, e.g. 6 h). With the use of the rainflow algorithm the temperature section is converted into a set of 2-tuple, which is visualized in a histogram plot. This outage is then executed with

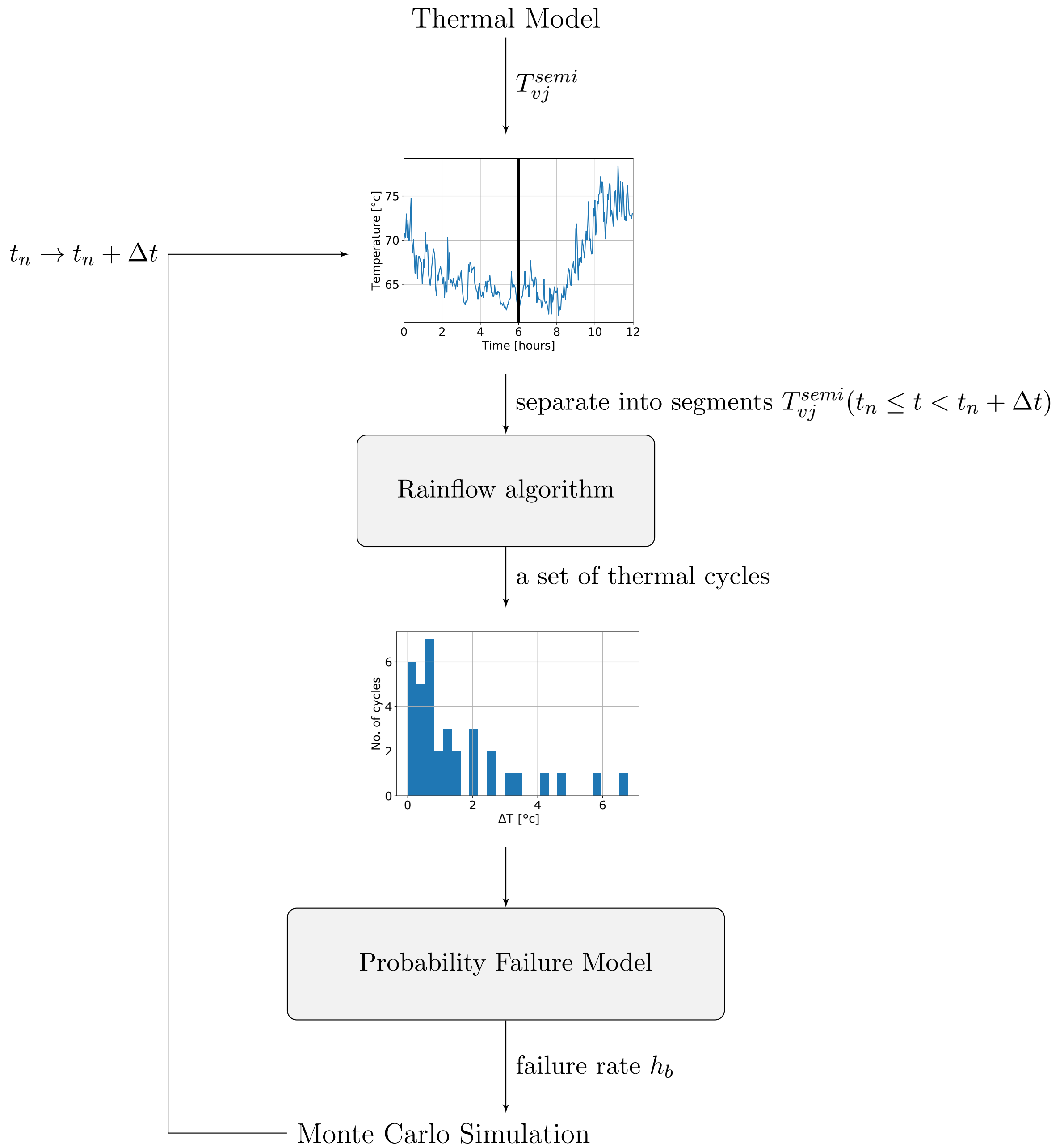

Figure 27: Conversion and simulation process visualized in a flow diagram, starting with the junction temperature and ending up with a loss prediction by the Monte Carlo simulation.

the probability failure model and generates the failure rate h_b for the random experiment. The Monte Carlo simulation calculates the number of outages based on the current time section. The progress for this section ends by storing the information for the lifetime prediction and increasing the time index to execute the algorithm for the following time section.

Rainflow algorithm The rainflow algorithm is a counter cycling method originally developed for the analysis of fatigue data. It computes closed hysteresis for a given stress history. The method was first proposed by [26] derived by an analogy from the rain flow (dripping off the pagonda roofs) and is meanwhile a well established method. Since then, many different formulations have been proposed in literature. [12,34] Beside this, other cycle counting methods are Peak Counting, Level Counting and simple range counting. [19] gives an overview and describes these methods. Nevertheless the rainflow algorithm has established itself as the most prominent and essential one because it considers, unlike other methods, the stress-strain hysteresis characteristic and can easily be applied to temperature data. [15]
The amplitude of a closed loop is defined by the pair of local maximum and minimum. [34] A distinction in the composition of the rainflow method is either the three-point algorithm, where the full history must be fixed at the beginning of the computation, or the four-point variant for a real-time analysis with a currently updated data set. In [27] a vivid and detailed rainflow algorithm analysis is given as well as a definition and visualization of the closed hysteresis.

Implementation of rainflow algorithm The rainflow is an essential part of the entire simulation. It reduces the junction temperature profile of the semiconductor into a number of closed hysteresis loops for the estimation of the fatigue damage. Looking back to Figure 27 brings to mind that the implementation processed a certain time series sequence for the range Δt periodically at each iteration step of the simulation. Therefore the rainflow algorithm is executed repeatedly with a new sequence $T_{vj}^{semi}(t_n \leq t < t_n + \Delta t)$ of the entire junction temperature profile. In order to consider the history of the process, the residuum of the previous execution step is stored and at the beginning of the rainflow progress the essential operating time series is (re-) initialised with the residue. The implementation for this thesis is visualized by the flow of Figure 28.

As shown in the flow chart, elements of the new sequence $T_{vj}^{semi}(t_n \leq t < t_n + \Delta t)$ are added element by element to the time series. This process forms an (outer) loop which ends the algorithm when all elements have been added and the residue of the time series is returned for an up-coming algorithm execution. The aim of the procedure is to identify closed loops in the time series, store these local maximum and minimum corner points which form this cycle and finally remove them from the series. For the detection of a loop, the four-point criteria is used and applied to the last section of the time series. If the four-point criteria is fullfilled, the loop-related values will be removed and the criteria will be evaluated again for the recent last section. This progress forms an inner loop and ends at least if the time series contain less than four data points. A simple preparation has to be done to enable the four-point criteria to be accomplished at all. The derivation must change from one point to the next. This can be validated every time a new element is added and the previous point removed or remained in the series.

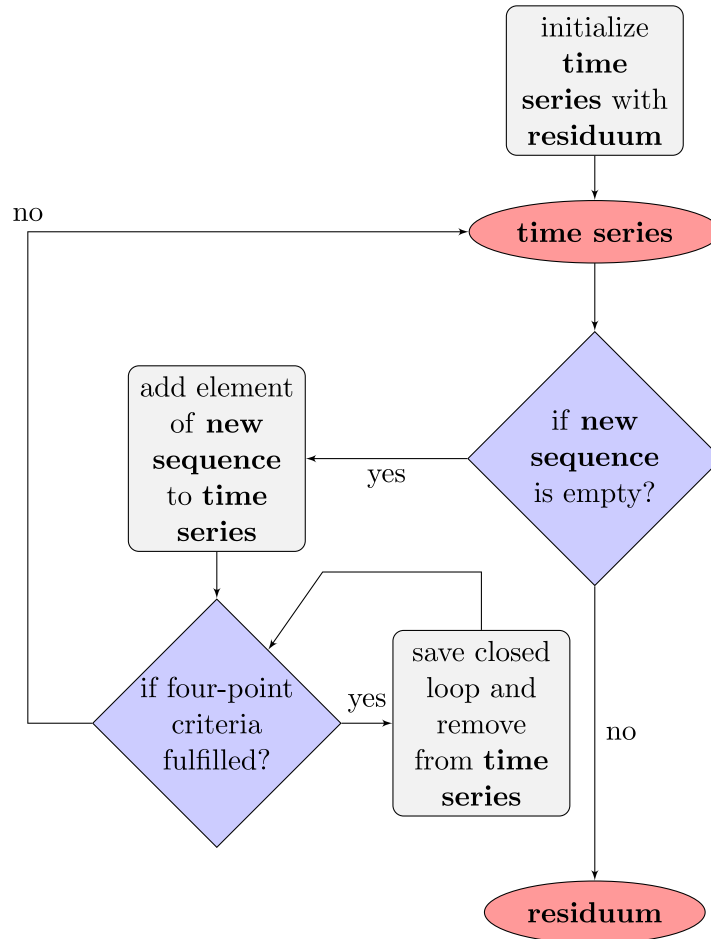

Figure 28: Rainflow implementation flow chart.

Four-point criteria The core part of the rainflow is the four-point criteria, applied to identify closed loops in a time series. Figure 29 illustrates an example of a closed loop and the detection of the criteria.

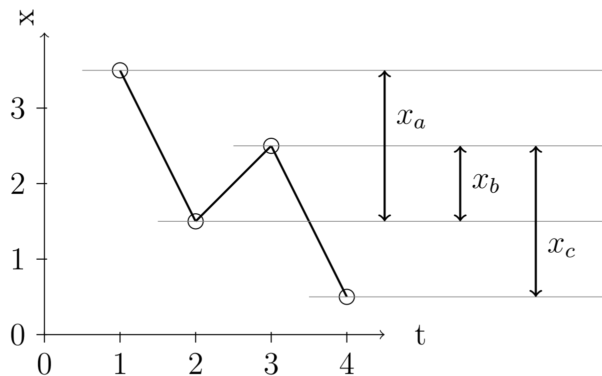

Figure 29: Outline of the four-point criteria. The criteria for a closed hysteresis loop is full filled if $(x_a \geqslant x_b)$ and $(x_c \geqslant x_b)$.

In a sequential series of four-points a closed loop with the amplitude x_b can be ascertained if ($x_a \geqslant x_b$) and ($x_c \geqslant x_b$). This illustration shows that the validation requires a continuous preparation to ensure a sequence with derivative change at each data point. Values in-between of an in- or decreasing sequence must be removed because they have no impact in forming a closed loop and inhibit the identification of the criteria.

Modeling of the probability failure model for bond wire fatigue In many previous works the lifetime approach for semiconductor bond-wire degradation bases on a linear accumulation model, like the Miner's rule (see section 2.4). It explains the degradation as a consumption of lifetime with each stress cycle. Two major limitations of this model are:

1. ignoring the probabilistic nature of fatigue,
2. simple linear life-stress relationship.

Certainly the outages follows a probabilistic distribution and are not reached after a fixed critical value of linear accumulation stress relation. [29]
Hence, for this thesis a more realistic failure model has been developed, inspired by [29]. Nevertheless, a couple of assumptions have to be made, derived from the previous publications [5, 29] and the IGBT application note specifications [17].
As a matter of principle, failure processes are usually Weibull distributed. Therefore, the major approach is to use the distribution for the model. The Weibull cumulative distribution function (cdf) $F(n)$ is given by

$$F(n) = 1 - e^{-(\frac{n}{\eta_b})^{\beta}_{b}} \quad , \tag{3.3.21}$$

with the scale parameter η_b and the shape parameter β_b.[6] The distribution is driven by the number of cycles n in distinction to the common parameter, time t. Certainly these two parameters η_b and β_b are unknown and have to be estimated. Unfortunately they can not be fully derived from measurements and application information because the provided failure statistics are limited. The lack of testing data requires some assumptions, derived from results of previous work. In the work of [5] power cycle tests for similar power components are performed, according to temperature swings up to 150 °C. By plotting the results for β_b of [5] in Figure 30 the linear relation

$$\beta_b(\Delta T) := k \times \Delta T + d \quad , \tag{3.3.22}$$

can be detected and the parameters computed with a fit with $k = -0.085\,°\mathrm{C}^{-1}$ and $d = 18.075$.

Regarding the small value set for the curve fit, another measurement performance for small values of ΔT might be possible, which would change the curve

[6]Note that there are many different conventions for the label definitions of the parameters in the literature.

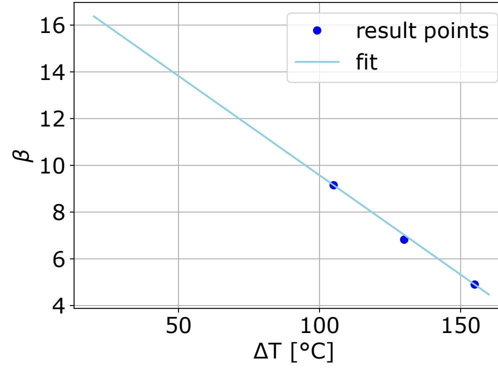

Figure 30: Linear curve fit for parameter $\beta_b(\Delta T) = k \times \Delta T + d$ of the Weibull distribution, with $k = -0.085\,°\mathrm{C}^{-1}$ and $d = 18.075$, considering results of [5].

progression in this area. But since the function values of β_b are still small and meaningful referred to the entire temperature range, the impact and deviation of the distribution behaviour is negligibly small.

A commonly accepted relation between number of cycles N_f and temperature gap ΔT is the Coffin-Manson law:

$$N_f = \frac{C}{\Delta T^\gamma} \quad . \tag{3.3.23}$$

It is used for the description of the scale parameter η_b, which is called the characteristic lifetime in Weibull distributions driven by time.

$$\eta_b(\Delta T) := \frac{C}{\Delta T^\gamma} \quad . \tag{3.3.24}$$

Nevertheless, there are more advances formulations but for this application is sufficient. In Figure 31 the B_{10} power cycling curve of the used IGBT module is plotted.

The dark blue line is extracted from [17], whereby the dotted path for $\Delta T < 40\,°\mathrm{C}$ is a manufacturer estimation. The sky blue line is a fit curve, which will be explained in the following section. The figure shows the curve's behaviour for 10% device losses.

Applying a logarithmic function on equation 3.3.24 leads to

$$\log(\eta_b(\Delta T)) = -\gamma \times \log(\Delta T) + \log(C) \quad , \tag{3.3.25}$$

which can be identified with the linear relation

$$\bar{\eta_b} = -\gamma \times \bar{\Delta T} + \bar{C} \quad . \tag{3.3.26}$$

The assumption that the dark blue curve in Figure 31b is basically a straight line and neglection of the slight change, simplifies Equation 3.3.26 to a linear

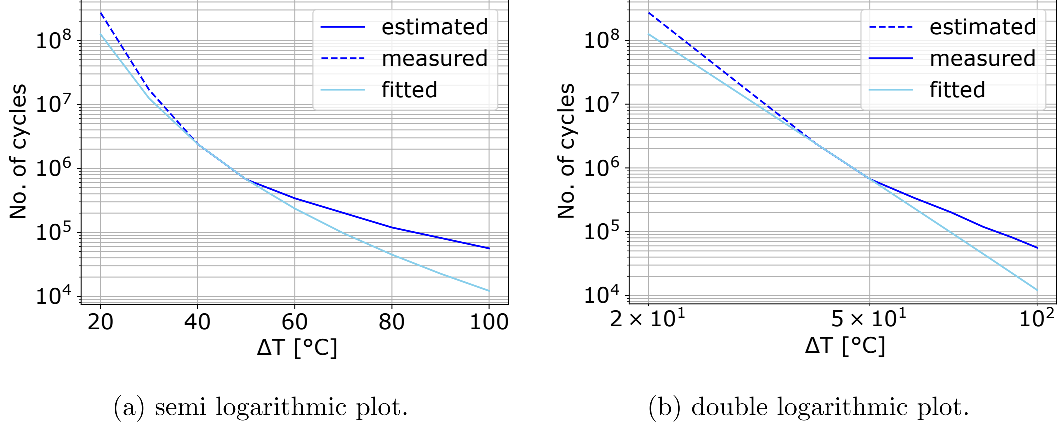

(a) semi logarithmic plot.

(b) double logarithmic plot.

Figure 31: Power cycling curve of the IGBT Module at $T_{vj,max}^{semi} = 125°c$ for 10% device losses. The dark blue curve composites of the estimated and measured values, extracted from [17]. The sky blue curve results of the fit, using the linear assumption for η_b.

equation with constant values for parameters C and γ. The changing gradient at $\Delta T = 40\,°\mathrm{C}$ could be considered in an advanced approach in future works with a varying γ. But since all values for $\Delta T < 40\,°\mathrm{C}$ are only estimations, the assumption of a constant value for γ is admissible at first. Nevertheless the result is highly related to the applied temperature profile. If the number of cycles is predominant in a range where the fitted line deviates from the power cycle tests, it has a high impact on the divergence of the lifetime simulation to the true value. Hence this effect, the range for a precise fit must be adjusted with the temperature profile. Regarding the mission profile in Section 4.3, the considered focus area for the fit is between 40 °C and 50 °C and the number of cycles for high values of ΔT is rather small.

In the following the Weibull cdf equation will be prepared and rearranged for the fit computation. Due to the limited testing data, only values for $F(n) = 0.1$ of [17] are available, which reduces Equation 3.3.21 to

$$0.1 = 1 - \exp(-(\frac{n}{\eta_b(\Delta T)})^{\beta_b(\Delta T)}) \tag{3.3.27}$$

$$\log(0.9) = -(\frac{n}{\eta_b(\Delta T)})^{\beta_b(\Delta T)} \tag{3.3.28}$$

$$\log(-\log(0.9)) = \beta_b(\Delta T) \times \log(\frac{n}{\eta_b(\Delta T)}) \quad . \tag{3.3.29}$$

Computing $\log(-\log(0.9)) \approx -2.25$ approximates the equation to

$$-2.25 = \beta_b(\Delta T) \times (\log(n) - \log(\eta_b(\Delta T))) \quad . \tag{3.3.30}$$

Divided by $\beta_b(\Delta T)$

$$-\frac{2.25}{\beta_b(\Delta T)} = \log(n) - \log(\eta_b(\Delta T)) \quad , \tag{3.3.31}$$

rearranges the formula to

$$\log(n) = -\frac{2.25}{\beta_b(\Delta T)} + \bar{\eta_b} \quad . \tag{3.3.32}$$

Simplified by using the previous assumptions for $\beta_b(\Delta T)$ and $\eta_b(\Delta T)$ result in

$$\log(n) = -\frac{2.25}{k \times \Delta T + d} - \gamma \times \log(\Delta T) + \bar{C} \quad . \tag{3.3.33}$$

Equation 3.3.33 depends on parameters ΔT and n, with fixed constants k and d (see Equation 3.3.22 and Figure 30) and not yet specified constants γ and $\bar{C} = \log(C)$. The extracted from values from [17] for n and ΔT provide all information for the curve fit process, especially in respect of the focused range between 40 °C and 50 °C, which has been visualized in Figure 31 with the sky blue curve. The results are the parameters $C = 3.5 \times 10^{15}\,°\mathrm{C}^{\gamma}$ and $\gamma = 5.678$ for the semiconductor bond-wire fatigue (Weibull) failure rate

$$h_b(n) = \eta_b^{-\beta_b} \times \beta_b \times n^{\beta_b - 1} \quad . \tag{3.3.34}$$

This model provides the essential failure rate for the Monte Carlo Simulation.

3.3.3 Monte Carlo simulation

The essential part of the simulation is the actual loss prediction. Starting with a set of inverters and their containing components, a step by step simulation predicts the losses at a particular time step. In the previous sections the modelling of fatigue mechanisms yields a probability to failure at a certain time. The determination of a fatigue is done by using a Monte Carlo random experiment based on the probability at that particular time.

Monte Carlo methods have a wide range of use especially in mathematical and physical problems, but in the last decades it has become famous as a decision-making tool for quantitative risk analysis. [13] For this thesis the Monte Carlo method is also used for the random experiment. Meaning to start with a probability for an event and determine a result by making a choice. The fatigue models yield a failure rate $h(t)$. The failure probability can be approximated by

$$P(t < T \leq t + \Delta t) \approx h(t) \times \Delta t \qquad \text{[28, p.36]} \tag{3.3.35}$$

For the Monte Carlo experiment the *numpy.random.rand(d1,d2,..,dn)* function[7] of the programming distribution Python is used. It creates random samples from a uniform distribution over [0, 1). In the following the snip of the Python Monte Carlo code is given.

[7] https://docs.scipy.org/doc/numpy-1.14.0/reference/generated/numpy.random.rand.html

Listing 1: Monte Carlo code

```
1  rand_sample = np.random.rand(num_left)
2  num_fail = np.sum(rand_sample <= P)
```

At the time step $t + \Delta t$, the dimension parameter $d1$ of function *numpy.random.rand(d1,d2,..,dn)* is set to the number of components *num_left* that are left and have not failed yet. The other optional parameters of the function remain bank and therefore unset. By comparing all numbers of the random sample *rand_sample* with the probability to failure P, the experiment is determined. If the random number is smaller or equal to the probability, the component determined to have failed. If not, it is the other way around. Every loss is labelled with the value one (true), the component that are left with a zero (false). Summing up the array of losses result in the number of components that have failed *num_fail* at this simulation step. The losses per time-step information must be stored for the upcoming evaluation.

Each component and failure mechanism of a system is executed separately. In this specific implementation the relation of components which belong to the system is not fixed during execution. The simulation ends if all components have failed or a scheduled time is reached. Then the components and their related lifetimes will be reassigned for an analysis to follow.

4 Analysis and discussion

In the first instance the analysis will be presented separately considering the single failure mechanisms. Each failure mode has its particular behaviour in context with individual parameters and resolutions which have to be analysed in detail independent of each other. After this reflection, the combined simulation of all (considered) components will be analysed and evaluated. In the following discussion a summary of the results, a conclusion and outlook will be given.

The validation of lifetime prediction methods is challenging and in some cases impossible. Primarily a comparison with authentic wear-out information is not feasible because inverter systems based on power electronic components did not exist some decades ago, hence the request for this lifetime prediction was given. Furthermore the confrontation with other works and publications is also intricate because applications and mission profiles are not equivalent, perhaps not even similar or comparable. Therefore the evaluation strategy has to split the validation into separate failure methods in the first instance and to validate or check them.

For a robustness validation of the design specification for the ASGC, the thermal model of the power electronic system has been used and an application-related mission profile, which have been presented and described in Section 3.

4.1 Electrolytic capacitor failures caused by degradation effect

Before using the thermal model to compute the electrolytic capacitor core temperature, the use of a simple assumption should help to explore and validate the behaviour of the universal failure method and the simulation. The approach for the core temperature is an oscillating temperature with the period of one day, modulated onto an average, constant temperature. The goal is to vary the constant temperature and the amplitude of the oscillation in order to analyse the properties of the simulation and compare the effect of the parameters.

$$T_{core}^{cap} = T_{constant} + T_{amplitude} \times \sin(2\pi \times \frac{t}{24\,\mathrm{h}}) \quad . \tag{4.1.1}$$

The use of parameters for a core temperature with a swing amplitude of $T_{amplitude} = 10\,°C$ and $20\,°C$ and a constant temperature $T_{constant} = 30\,°C$, $50\,°C$ and $70\,°C$ is visualised in Figure 32. The labels in the legend are composited with the amplitude first and the constant parameter second after the letter p(plus) representing an additional term.

The simulation results are presented in Figure 33a with an amplitude $T_{amplitude} = 10\,°C$ and Figure 33b with $T_{amplitude} = 20\,°C$. The results seams reasonable and consistent, for instance an increasing amplitude implies a shorter lifetime.

The figures show the earliest failure for the highest (constant) temperatures, in Table 5 some key figures have been extracted in order to compare the two plots. The 1% mark of component that have failed is introduced as the lower limit, the 99% mark as the upper and η_c as the characteristic lifetime.

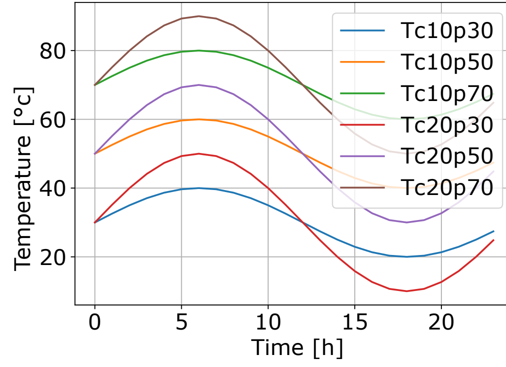

Figure 32: Simple core temperature approach of oscillating temperature with the period of one day.

	$T_{amplitude} = 10\,°C$			$T_{amplitude} = 20\,°C$		
$T_{constant}$[°C]	$t_{1\%}[y]$	$\eta_c[y]$	$t_{99\%}[y]$	$t_{1\%}[y]$	$\eta_c[y]$	$t_{99\%}[y]$
70 °C	7 – 8	13	11 – 22	3 – 5	8	9 – 10
50 °C	46 – 57	91	103 – 114	22 – 34	47	57 – 69
30 °C	342 – 456	781	913 – 1027	114 – 228	346	342 – 457

Table 5: Key figures of result for simple core temperature model.

It can be observed that the variation of the constant term shifts the failure curve by about one magnitude. On the other side the shift triggered by the different temperature swing amplitude is only in the scale of a single-digit factor. This investigation also shows that meaningful failures times result of constant temperatures $T_{constant} > 50\,°C$.

In the next step the mission profile will be used with results following. As described in Section 3.2.3, the heating of the capacitor is driven by the electric current and therefore the sun radiation and the balancing of asymmetric grid loads. It has been distinguished between a single operation of radiation or balancing and a combined mode with prioritization (in order to handle over-stressing of phases). By applying the mission profile with radiation conversion priority to the thermal model of the electrolytic capacitors, the core temperature for the component can be computed. Figure 34a shows the course of the core temperature. Also the ambient temperature is represented as well.

To analyse the comparison between ambient and core temperature, Figure 34b shows the histogram of the temperature difference. Clearly detectable is an average temperature gap of about 10 °C and a maximum of 20 °C. The average temperature of Figure 34a can be computed and amounts to 20.92 °C. Looking back to Figure 33 indicates that the approach of $T_{amplitude} = 10\,°C$ is appropriate but the assumptions for $T_{constant}$ seems to high. Nevertheless this shows already that the failure times will be quite high. Figure 35 shows the results for the electrolytic capacitors by using the mission profile and distinct (priority-)settings.

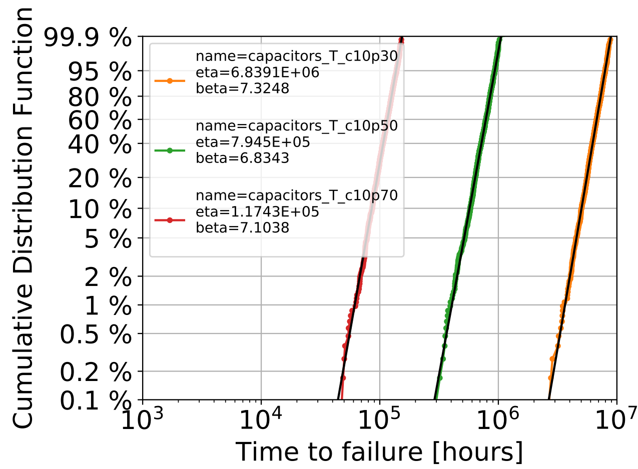

(a) Swing amplitude 10 °C; Positioning: ltr (left to right)

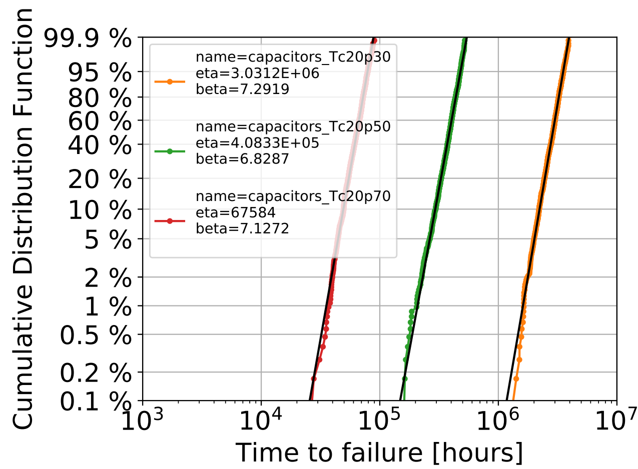

(b) Swing amplitude 20 °C; Positioning: ltr

Figure 33: Weibull plots of electrolytic capacitor results for a simple core temperature approach. Simulation parameters: dt=6h, SPH=1h

It can be observed that the combined option leads to higher stress and earlier fatigue times. Interestingly the grid balancing means higher stress to the components than the radiation. This fact seams meaningful because asymmetrical grid components imply a with higher ripple current terms compared to the symmetrical radiation. Moreover it can be seen that the difference between the priority options is pretty small but the radiation prioritization means slightly more load stress. This circumstance is noteable especially because the results without combination were the other way around. In order to validate these outcomes, the results can be compared with Figure 33 and Table 5. As mentioned before, the average temperature of the core temperature by the mission profile is smaller than $T_{constant}$ in the simple model. Due to this fact, the stress must be less and the outage times greater, which can be verified. Indeed failure time depend on the

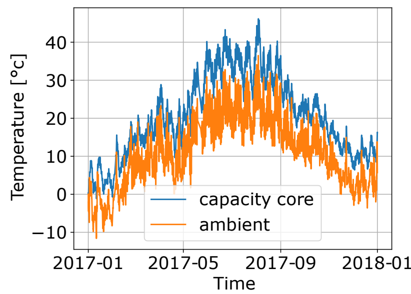

(a) Temperature Course.

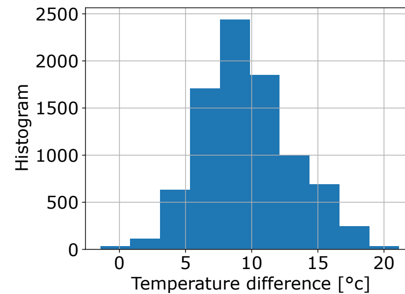

(b) Histogram of temperature difference.

Figure 34: Core temperature of the electrolytic capacitors resulting of the mission profile for one year.

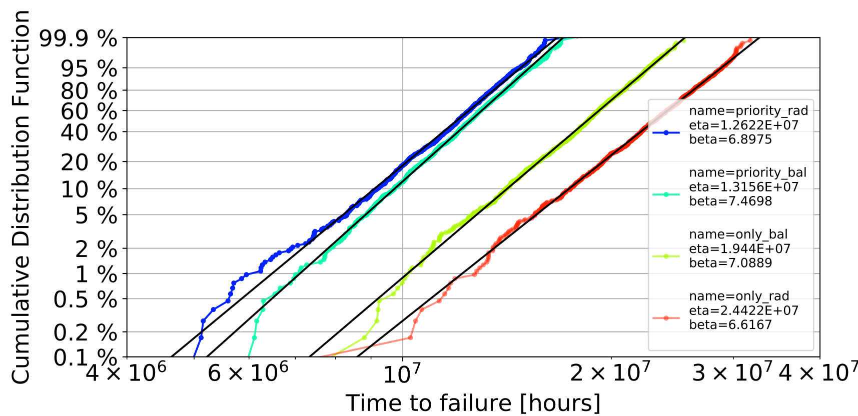

Figure 35: Weibull plot for electrolytic capacitors with distinct priority-settings; Positioning: ltr; Simulation parameters: $dt = 6\,\mathrm{h}$, $SPH = 1h$.

operation area and application but typical outage times of electrolytic capacitors are in a range of $15y - 25y$. Obviously the failure times of the simulation are much higher. This divergence to typical failure times could be caused by the mission profile (e.g. application or operation area) as well as the established model for the electrolytic capacitor. Therefore the mission profile will be modified with an increasing stress-trigger to resolve this question and analyse the behaviour. In Figure 36 a segment of a test signal is shown, which has been used as a radiation profile instead of the original mission profile.

In addition some fictive scenarios have been created with a permanent maximal radiation or an entire asymmetric grid (where all phases have the exact same angle). The designed radiation or load information have replaced one time series of the mission profile. In figure 37 the temperature courses of the modified mission profiles can be seen.

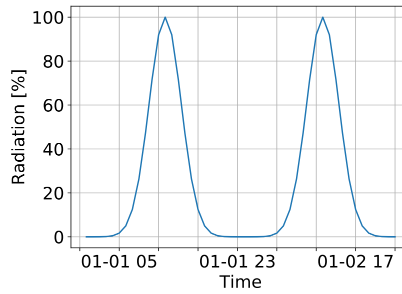

Figure 36: Segment of test signal for electrolytic capacitor's core temperature.

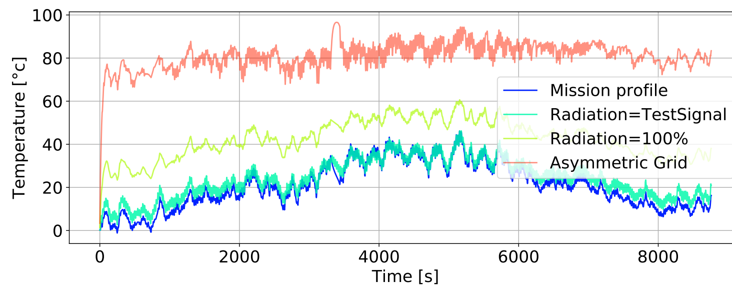

Figure 37: Temperature course of electrolytic capacitor for modified conditions.

The permanent radiation already shows an pretty big deviation, but the asymmetric grid surpasses this course by far. These distinct temperature behaviours result in the simulation results in Figure 38.

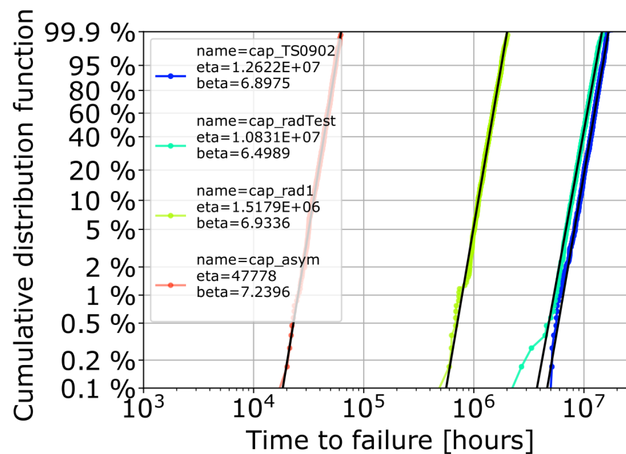

Figure 38: Weibull plot for electrolytic capacitors with various mission profile scenarios; Positioning: rtl; Simulation parameters: $dt = 6\,\text{h}$, $SPH = 1h$.

The Weibull curve of the asymmetric grid has been shifted to a characteristic lifetime η_c of about 5.45 y. This is obviously an overstress and fictive scenario and therefore faraway of the other results. But beside an overdesigned system for the

small loads of the original mission profile, the actual results show that all realistic scenarios lead to failure times much higher than typical comparables. Therefore it has to be concluded that the model is not appropriate for the analysis of the electrolytic capacitors in this application. To get more reasonable predictions the model has to be modified. This could be done with further characterization measurements to validate the model assumptions but also with additional failure mechanisms.

An interesting question is how the results change by varying the resolution (samples per hour) of the primary input series or the modification of the simulation steps (dt). For the following simulations, the mission profile has been composed of radiation and balancing data with radiation priority setting. The variation of samples per hour can be studied in Figure 39 with a fixed step size $dt = 6h$. With the change of the SPH the mission profiles will be generated with a higher resolution. This could result in a slightly different delayed core temperature caused by the thermal capacity. The resolution is limited by the input series of the mission profile and an interpolation is not target-aimed.

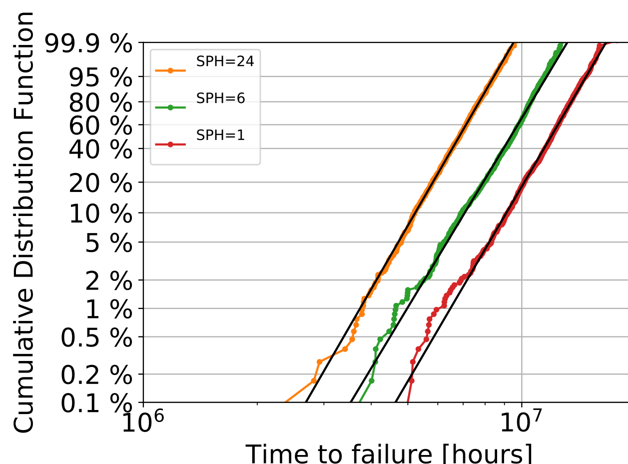

Figure 39: Weibull plot for electrolytic capacitor with varying mission profile resolution SPH; Positioning: ltr; Simulation parameter: $dt = 6\,\mathrm{h}$.

It can be ascertained that the resolution of the mission profile has impact on the outcome. A more precise input series lead to slightly shorter outage times. Nevertheless the gap between $SPH = 1$ and $SPH = 24$, which is a resolution of 1 h compared to 180 s is a shift of $t_{1\%} = 1300y$ to $2600y$. This corresponds to a doubling but an outage time which exceeds the expected operation time by far. Another interesting research subject is the variation of simulation steps dt. Therefore the steps are changed from $dt = 1\,\mathrm{h}$ until $dt = 12\,\mathrm{h}$ with fixed $SPH = 1$. This means that the mission profile is generated with one step per hour and the simulation takes each step for $dt = 1\,\mathrm{h}$ or skips several. Figure 40 shows the simulation results for $dt = 1$, 3, 6 and 12 h.

The result is obvious and therefore the conclusion simple. The variation of simulation steps do not effect simulation result. This fact is interesting because

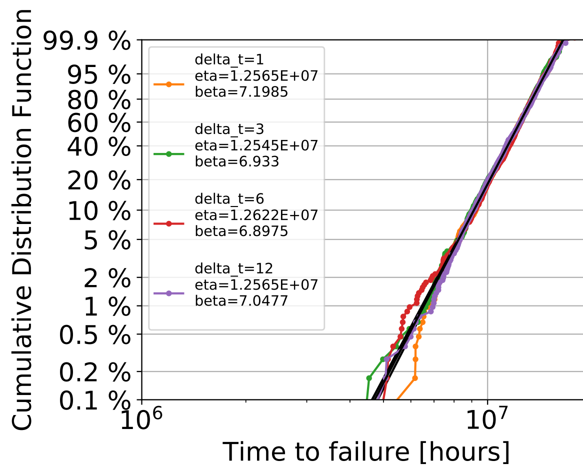

Figure 40: Weibull plot for electrolytic capacitor with varying simulation step size; Simulation parameter: $SPH = 1\,\text{h}$.

the temperature changes in the course of the day. But obviously the impact is to small or the higher step sizes affect like an average value and the spread of temperature in-between cancels.

4.2 Semiconductor failures caused by cosmic radiation

The essential parameter for the cosmic radiation is the altitude above the altitude above the sea level and therefore also for the failure model. Moreover the other relevant parameter is the junction voltage V_{DC}. These two input factors are fixed for a specific mission profile, nevertheless the following section considers a variation of the parameters. Figure 41 shows the failure in time (FIT) for changing voltage and comparing various values of the altitude above the sea.

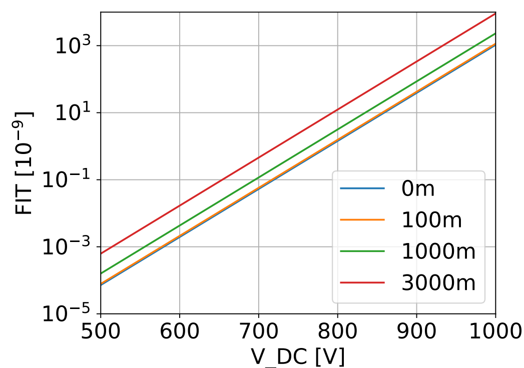

Figure 41: Semiconductor cosmic radiation failure in time (FIT) curve.

Notable is that the FIT values change in a logarithmic scale by varying the voltage from 500 V to 1000 V. Certainly this behaviour has already been described with Equation 3.3.16 and 3.3.17 but is illustrated by this Figure.

The junction temperature of the semiconductor results by applying the mission profile to the thermal model. In Figure 42a the temperature course is illustrated and by way of comparison the ambient as well. Conspicuously, the amplitude of the temperature swings is enlarged and the gap is at least 65 °C. This can be seen in Figure 42b, where the temperature gap has been evaluated in a histogram plot for each time point.

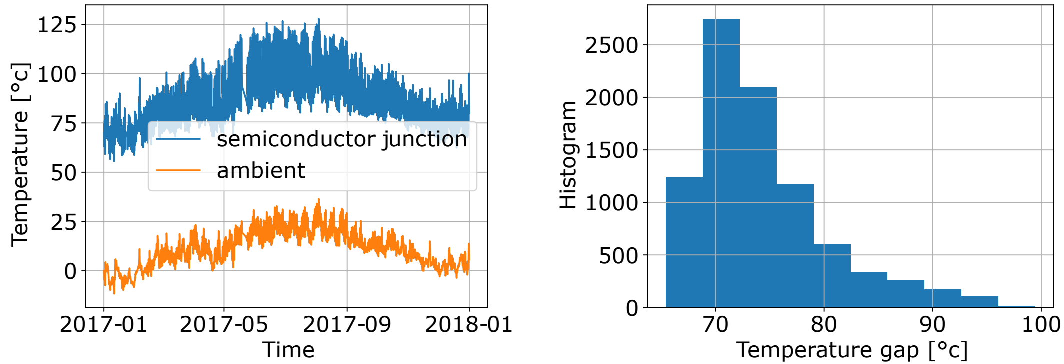

(a) Temperature Course.

(b) Histogram of temperature difference.

Figure 42: Semiconductor junction temperature with the use of the application mission profile.

By the variation of the two parameters, the distinct impacts and changes of the FIT has been evaluated. This information can be used to validate or at least classify the results of the simulation. Therefore Figure 43 visualizes the modification in a bar plot for the minimum and maximum of the junction temperature.

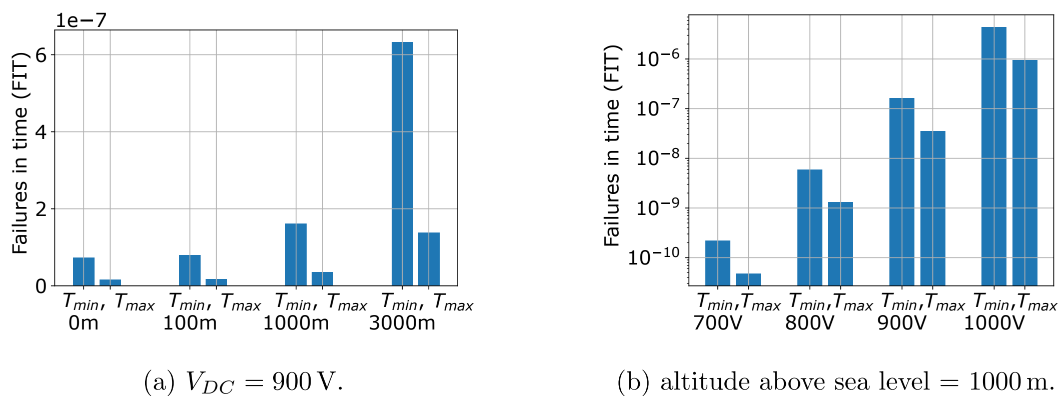

(a) $V_{DC} = 900\,\text{V}$.

(b) altitude above sea level = 1000 m.

Figure 43: Semiconductor cosmic radiation using mission profile under the variation of parameters V_{DC} and altitude above sea level.

Looking at the changing of FIT by varying the altitude above the sea level shows an alteration within the range of one magnitude. Moreover the gap between

$T_{min} \approx 56\,°\mathrm{C}$ and $T_{max} \approx 128\,°\mathrm{C}$ occurs also in this span. The altitude steps size do not obey a certain regulation. Sea level zero represents the lowest and therefore the reference point, 100 m is roughly the altitude of Vienna, Austria (where the mission profile information has been recorded) and 1000 m respectively 3000 m are two more benchmarks of a fictional highland or mountain.
A variation of the junction voltage V_{DC} changes the FIT in several magnitudes, which can be seen in Figure 45. The junction voltage $V_{DC} = 700\,\mathrm{V}$ result in FIT rates in the order of 10^{-10}, which is very unlikely and causes quite long simulation times. This little insight into the behaviour of the FIT function by varying the parameters offers the possibility of a result validation for the actual simulation.

In the following the proper simulation results will be presented. The fixed parameters for the thesis are

$$V_{DC} = 900\,\mathrm{V} \quad , \tag{4.2.1}$$

$$\text{altitude above sea level} = 100\,\mathrm{m} \quad , \tag{4.2.2}$$

$$\tag{4.2.3}$$

corresponding to the location of Vienna, Austria, where the root information for the mission profile have been recorded. Figure 45 shows the result and compares the plots for different sea levels and a fixed junction voltage V_{DC}.

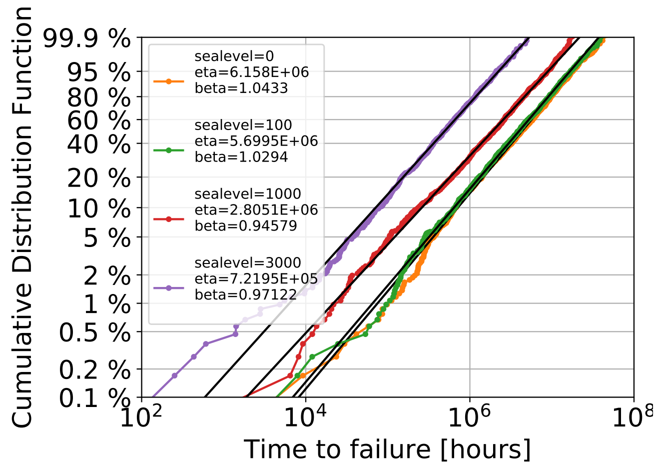

Figure 44: Weibull plot for semiconductor cosmic radiation with junction voltage $V_{DC} = 900\,\mathrm{V}$; Positioning: rtl; Simulation parameters: $dt = 6\,\mathrm{h}$, $SPH = 1$.

In Table 6 the key data of the Weibull plot is listed.

It is discernable that the time information ($t_{1\%}$ as well as $t_{99\%}$) for the distinguished sea levels is close-by. These facts can be reviewed with the conclusion of Figure 43a and seam reasonable. The failure curves start soon in the magnitude between $1 \times 10^1\,\mathrm{y} - 3 \times 10^3\,\mathrm{y}$ but end pretty late. This low gradient result in smaller β_c values, compared to the electrolytic capacitors. Nevertheless the effect occurs quite early and after 22 y already 1% of the semiconductor components have failed caused by cosmic radiation.

altitude above sea level	$t_{1\%}[y]$	$t_{99\%}[y]$
0 m	24	8500
100 m	22	8500
1000 m	7	4600
3000 m	2	2000

Table 6: Key data for mission profile based semiconductor cosmic radiation failures by varying the altitude above the sea level.

In Figure 45 the variation of the junction voltage V_{DC} was tested.

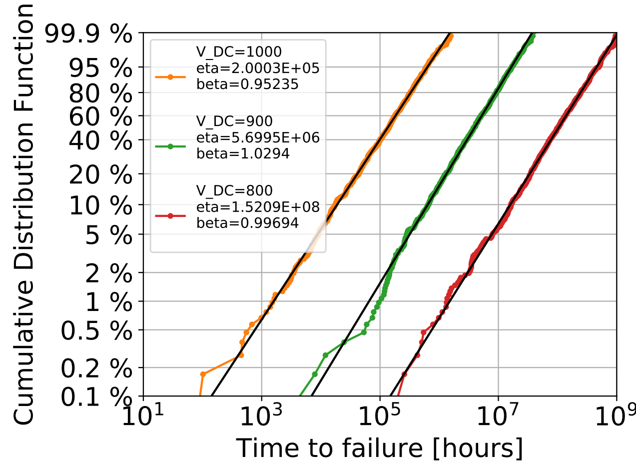

Figure 45: Weibull plot for semiconductor cosmic radiation with altitude above sea level = 100 m; Positioning: ltr; Simulation parameters: $dt = 6\,\text{h}$, $SPH = 1$.

In comparison to the variation of the sea level, a wider diverge is identifiable for the junction voltage V_{DC}. This observed pattern can be verified and approved with results of Figure 43b. In Table 7 the key data has been summarized. Voltages smaller than $V_{DC} = 800\,\text{V}$ have not been simulated because the computation time increases excessively with dropping voltage.

junction voltage V_{DC}	$t_{1\%}[y]$	$t_{99\%}[y]$
1000 V	0.5	340
900 V	22	8500
800 V	514	244500

Table 7: Key data for mission profile based semiconductor cosmic radiation failures by varying junction voltage V_{DC}.

As described, key data shows an early occur of failures but especially a sensitive reliance for voltage changes. A rising voltage of 100 V from 900 V to 1000 V changes the $t_{1\%}$ value for the semiconductor failures from 22 y to 0.5 y. This shift

also implies a high probability of failure in the maximum operation time and is therefore an essential outage mechanism which should be observed closely.

Finally the change of the sample rate SPH has been investigated for this module as well in Figure 46.

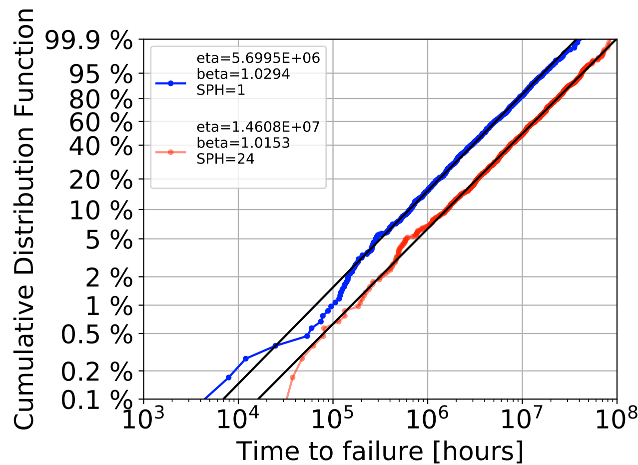

Figure 46: Weibull plot for semiconductor failures caused by cosmic radiation considering varying sample rate SPH; Positioning: ltr; Simulation parameters: $dt = 6\,\mathrm{h}$

It can be observed that both results are close-by but an increasing sample rate SPH also increases the failure times.

4.3 Semiconductor failures caused by thermo-mechanical stress

The analysis and verification of the thermal-mechanical model is of major interest because the fundamental concept is new and has not been developed and implemented yet, except of [43] with a distinct approach. Therefore the focus is on an extended algorithm validation, before presenting the actual simulation results. In the beginning the implemented algorithm will be verified by customized test signal. The result will identify particular limitations of the method and the implemented simulation. After that, the mission profile will be applied to the algorithm, therefore predictions can be made and conclusions and some outlook will be given.

Algorithm validation For the validation of the model, a well defined input should be applied in order to verify the outcome. This is especially necessary for this newly developed module where no comparable results are available. Hence this, some simple temperature input signal has to be selected and prepared, wherefore the results are known. With regard to the adjustment of the model parameters in Figure 31 and discussed in Section 3.3.2, temperature signals with a peak-to-peak amplitude in the range of 40 °C to 50 °C are meaningful. For a

start, a simple sinus signal with the specified amplitude seems suitable. Due to the limited resolution of the signal it turns out that the desired outcome requires steep signal edges which can be provided by a rectangular wave. In Figure 47 a set of signals with a temperature gap of $\Delta T = 40\,°\mathrm{C}$ is illustrated.

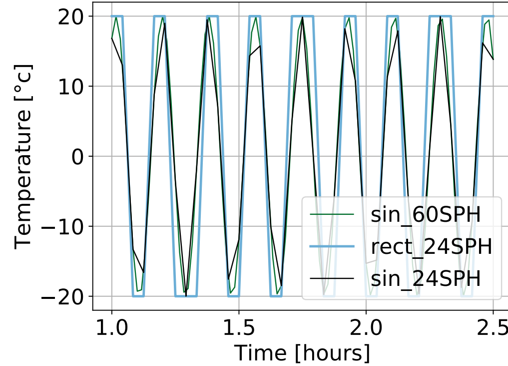

Figure 47: Snippet of test signals for the semiconductor bond-wire fatigue module with a temperature gap of $\Delta T = 40\,°\mathrm{C}$.

The resolution for the simulation is defined with steps per hour (SPH) which results in a segmentation of the time scale. The inverse behaviour implies that the higher the SPH rate is, the smaller the time steps are.
The signal frequency f is adjusted so that after 50 years of simulation, 2.4×10^6 cycles are reached which is equivalent to 10% losses:

$$f = \frac{2.4 \times 10^6}{50 \times 365 \times 24}\,\mathrm{h}^{-1} \quad , \tag{4.3.1}$$

with reference to the power cycling specifications in Section 3.3.2.

The mathematical formulation for the signal is

$$20 \times \sin(2\pi f \times t) \quad , \tag{4.3.2}$$

with time unit hours. The signals have been applied to the rainflow algorithm as a mission profile. Figure 48 shows the results of the rainflow algorithm plotted in a histogram plot. It can be observed that depending on the signal form and the SPH the results are are distinctively distributed and spread over the histogram.

Both, signal form and SPH have an effect on the rainflow results. A low resolution leads to a shift and a separation towards smaller temperature gaps. The study of Figure 47 already makes clear that the downscaled resolution separates the single-frequency sine signal into several frequency components. This circumstances affect the subdivided bars in the histogram results.

In respect of the power law behaviour of η_b in Equation 3.3.24, even a small variation in the single-digit range of ΔT can finally lead to a shift up to several years in the simulation results. Obviously a higher resolution could solve this problem but by increasing the SPH, the execution time of the simulation is getting

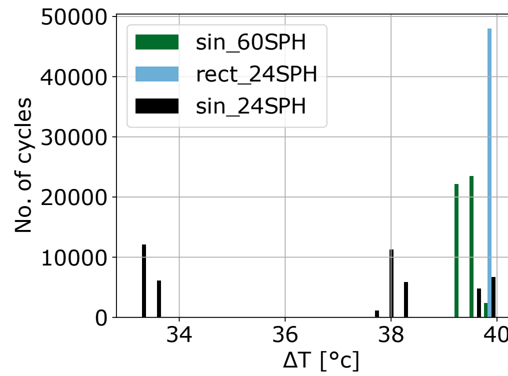

Figure 48: Histogram of rainflow algorithm results for temperature test signals and a time range of one year.

longer. A balance between computation time and resolution has to be achieved. Hence the use of the rectangular function is an alternative solution, certainly only for test signals.

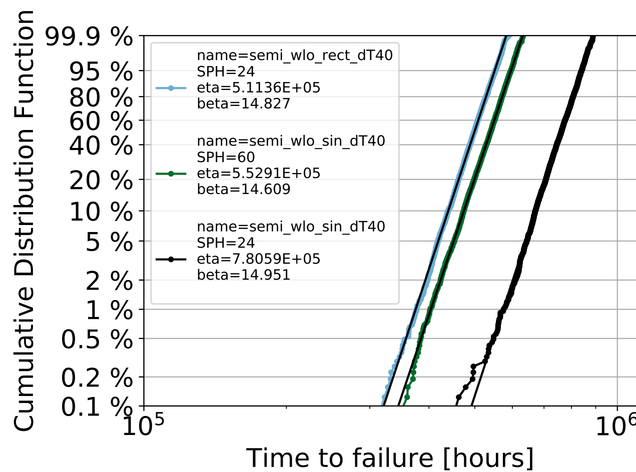

Figure 49: Weibull distribution of semiconductor bond-wire fatigue for test signals. The result of the rectangular signal at 10% cdf correspond with 2.4×10^6 with the power cycle specification. The results of the sine signals are shifted because of their low resolution.

In this preceding validation section sample rates of $SPH = 24$ and $SPH = 60$ have been applied because otherwise 2.4×10^6 power cycles in 50 y could not have been achieved. The idea was to use a single-frequency signal in the center of the focus area ($\Delta T = 40\,°\mathrm{C}$) which necessarily results in a high frequency and therefore SPH rate. For the previous failure mechanisms and simulations in particular sample rates of $SPH = 1$ have been used in respect to the increasing execution time. In the upcoming session this subject will receive raised attention.

The last exploration subject of the validation sector will be the probability distribution behaviour of the developed failure module. Therefore in Figure 50 the

cumulative distribution function $F(n)$ has been plotted, by considering various temperature gaps ΔT, starting from 10 °C to 100 °C.

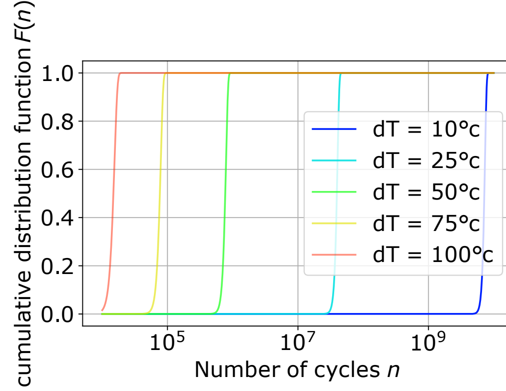

Figure 50: Cumulative distribution function $F(n)$ for the semiconductor bond-wire fatigue modul with various temperature gaps ΔT.

It can be seen that the x-axis marking is logarithmic which is related to the power cycling behaviour, shown in Figure 31b. The rise and gradient for $F(n)$ is rapid but with regard to the logarithmic setting. This fact indicates quite high values for the Weibull scale parameter β_b. This circumstance can be verified with the validation results of the test signals in Figure 49 compared to the β values of the other two failure modules with $\beta_c \approx 1$ for the cosmic radiation and $\beta_e \approx 7$ for the electrolytic degradation.

Mission profile results To investigate the semiconductor bond-wire fatigue effect for a specific operation, the mission profile of Section 3.1 has been applied. Before showing the simulation result, the rainflow will be applied to the mission profile and the outcome analysed for the purpose of parameter selection, recognizing critical variations and validating the simulation result. The result of the rainflow is a set of tuples, composed of the temperature difference ΔT and the number of cycles n. To extend the plot and increase the lucidity, an additional axis with the mean temperature

$$T_m = T^i_{min} + \frac{\Delta T}{2} \quad , \tag{4.3.3}$$

$$\Delta T = T^i_{max} - T^i_{min} \quad , \tag{4.3.4}$$

has been added, whence a 3d-histogram results. Figure 51 shows the results of the rainflow algorithm with distinct SPH rates.

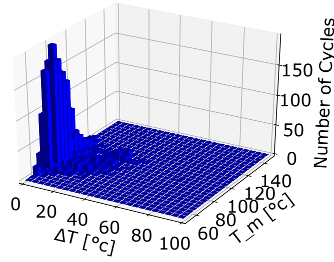

(a) $SPH = 1$

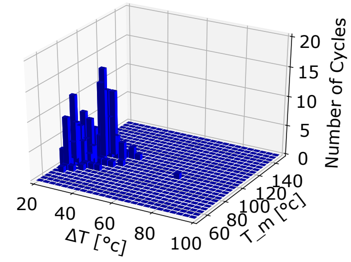

(b) $SPH = 1, \Delta T > 20\,°\mathrm{C}$

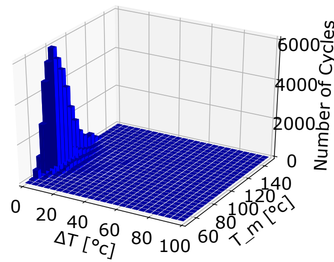

(c) $SPH = 24$

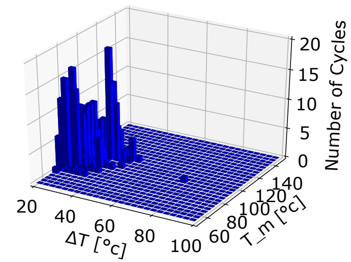

(d) $SPH = 24, \Delta T > 20\,°\mathrm{C}$

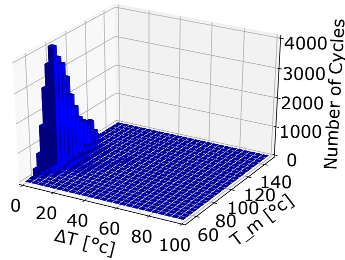

(e) $SPH = 60$

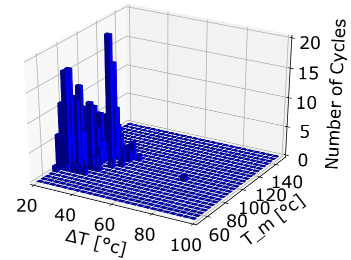

(f) $SPH = 60, \Delta T > 20\,°\mathrm{C}$

Figure 51: 3d-histogram of rainflow results for mission profile of one year with distinct SPH rates.

The comparison of Figure 51a, 51c and 51e unambiguously shows a fast increase in the number of cycles for higher sample rates. Figure 51b, 51d and 51f show the same histogram but consider only temperature differences $\Delta T > 20\,°\mathrm{C}$. All three figures illustrate a very similar picture. That clarifies that this massive change only takes place for small temperature gaps, which are obviously caused by the increasing resolution wherefore slight variations appear and are detectable. In this scenario, the raw input data for the system characterization module is always the same but the output sample rate SPH has been modified. A smaller resolution therefore neglects small ups and downs. The sample limit is at least reached with $SPH = 60$ because the weather data has a time resolution of 1 min and

the load profiles of $180\,\mathrm{s} = 2.5\,\mathrm{min}$. Further increase of the sample rate would just involve interpolation of missing values and therefore add errors to the data instead of additional information. These two sample rates might be the reason of the uncertain reduction of the number of cycles by the increase from $SPH = 24$ to $SPH = 60$. Perhaps variations of weather and load data interfere with this change and may have chanced one another. Therefore in future works the use of a different mission profiles for another application or climate zone would be reasonable.

After this pre-investigation, the following mission profiles have been used for the simulation by considering the explored parameters $SPH = 1$ and $SPH = 24$. $SPH = 60$ has not been used because the results were similar to $SPH = 24$ and the computation time rises drastically. In Figure 52 the simulation outcome has been visualized in a Weibull plot.

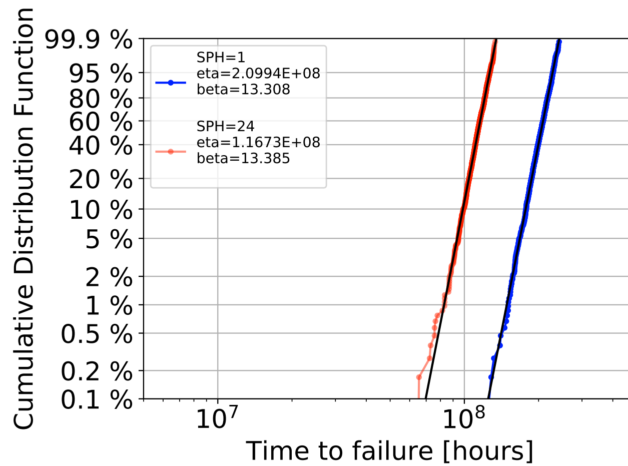

Figure 52: Weibull distribution plot of semiconductor failure caused by bond-wire fatigue with varying SPH; Simulation parameters: $dt = 6\,\mathrm{h}$.

When comparing the β-values of the other failure mechanism simulations, it can be seen that the results are relatively high, with $\beta_b \approx 13.3$-values. Despite this fact, the η_b-values as well as the $t_{1\%}$ and the $t_{99\%}$ times are rather high and with values way above 1000 years not relevant to consider for a system outages.

4.4 Overall simulation results

In the previous sections, the failure modules have been separately validated, verified and analysed. For an outage of the system the overall treatment is certainly necessary. For an overall result, all the outcomes have been rearranged by selecting failure times of the modules and have been randomly matched to a fictive systems. The minimum failure values for each system are relevant, because only a single component failure implies a system outage. In Figure 53 all Weibull plots and the combined result are visualized.

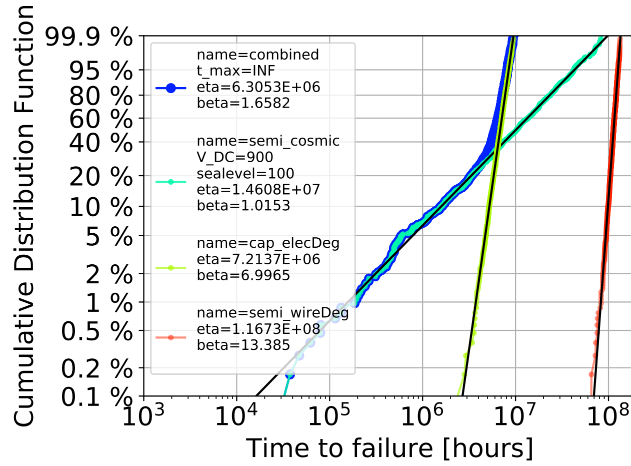

Figure 53: Weibull plot of the entire system; Positioning: ltr; Simulation parameters: $SPH = 24$, $dt = 4\,\text{h}$.

It is shown that in the first instance the failures caused by cosmic radiation dominate the Weibull cumulative distribution function (cdf). Just when the electrolytic degradation subtend the cosmic radiation line, the entire curve bends. Therefore the electrolytic degradation dominates the system outages at a cumulative failure of $cdf \approx 40\%$. This occurs at failure times $t_{40\%} \approx 800\,\text{y}$. Just as the failure curve for the semiconductor bond-wire degradation is way above and in the considered range until $t_{99.9\%}$ not relevant at all.
Therefore this figure shows that in the designated operation time the semiconductor failures caused by cosmic radiation are responsible for system outages regarding the conditions specified in the mission profile and models. Nevertheless, as already concluded, the failure times for electrolytic capacitors are not realistic, so that this capacitor model is not appropriate for this application.

5 Summary, conclusion and outlook

Summary In this thesis a robustness validation of the design specification in particular for the AIT Smart Grid Converter (ASGC) has been developed by initially exploring the essential weak components and their main failure mechanisms. For the purpose of design universal validation methods but adjusted to the specific photovoltaic converter application, the implementation has been split into separate parts.

The first part contains system specific thermal models for the semiconductors and the electrolytic capacitors, the weak components of the system. In a nutshell the task of the thermal models is to provide thermal component data by applying the mission profile of the operation field as an input to the simulation. The models have been derived by a full-load characterization measurement of the ASGC system. The result yields a thermal capacity for the electrolytic capacitor's thermal model but not for the semiconductor. This behaviour has been determined by the delayed temperature rise and modelled with an exponential function. In general the thermal models for the components have been developed by temperature junctions, starting with the environment ambient temperature and continually adding temperature transition steps at each system section. The temperature gaps are affected by heat production due to power loss of the system in addition to a fixed temperature offset. These settings and adjustments incorporate beside the thermal measurements insight knowledge of the schematics and application note.

The second part consists of universal failure models and a lifetime simulation which leads to the loss prediction. In this thesis the bond-wire fatigue and cosmic radiation failure for the semiconductors have been considered as the essential failure mechanisms, as well as the electrolyte degradation of the electrolytic capacitors. The semiconductor bond-wire degradation development has been challenging due to the lack of statistical results. Hence additional assumptions have been made based on previous publications. Model approaches for the remaining failure mechanisms already existed, which have been combined, adapted and adjusted. The failure models yield the failure rate, depending on the component temperature as an input.

The use of a fictive set of systems (respectively their components) and an offline mission profile enables the possibility for an accelerated life simulation and loss prediction.

Conclusion The results of the robustness validation for the AIT Smart Grid Converter (ASGC) design specification base on the mission profile for specific application as a photovoltaic power converter. The profiles consist of offline weather data and load profiles of Vienna, Austria 2017. The simulation shows an overdesigned system for this application with less than 10% system wear-outs after 100 years and semiconductor failures due to cosmic radiation as the most likeliest mechanism. The slowly increasing failure rate of the cosmic radiation is replaced for long operation times in the range of $400-800\,years$ by the electrolytic

capacitor degradation, which finally dominates the statistics until all systems have worn out. Nevertheless the failure time for the electrolytic capacitor model deviates from typical reference values for this application. It has to be concluded that the capacitor model is not appropriate to achieve a realistic prediction in this scenario. Additional failure mechanisms as well as further system measurements and load profiles scenarios should lead to an advanced failure model.

Reflection and outlook The thermal model design has to be done with sparse measurement results. By considering more measurements with distinct loads and experimental scenarios, more progress could be made and an advanced model created. Moreover an extended experimental setup could enable the possibility to distinguish between the component regarding their location and include this into the simulation (e.g. FEM simulation).

Furthermore number and size of the electrolytic capacitor array is overdesigned but the lifetime results are too high in comparison to reference values. Therefore the model is not appropriate and must be adapted for realistic lifetime predictions. Additional failure mechanisms have to be considered or the model assumptions have to be evaluated by further system measurements. The divergence could also be caused by the model reduction of the entire array to equal capacitors and a unique behaviour. An asymmetrical capacitor load and therefore permanent overstressing would also lead to shorter failure times. This issue could also be investigated by additional measurements.

In addition the use of another mission profile for a different application of operation area (e.g. climate zone) could be reasonable in order to compare distinct load results.

In future works the implementation could be extended to real-time applications to ensure predictive maintenance or further develop the system design and avoid bottlenecks at failure sensitive components or overstress.

References

[1] The Weibull Distribution - ReliaWiki.

[2] Military Handbook: Reliability Prediction of Electronic Equipment, December 1991.

[3] ABB. Application Node 5SYA 2042-0 - Failure rates of IGBT modules due to cosmic rays, 2017.

[4] Arne Albertsen. Electrolytic capacitor lifetime estimation. 2010.

[5] R. Amro, J. Lutz, and A. Lindemann. Power cycling with high temperature swing of discrete components based on different technologies. In *2004 IEEE 35th Annual Power Electronics Specialists Conference (IEEE Cat. No.04CH37551)*, volume 4, pages 2593–2598 Vol.4, 2004.

[6] Sanjeev Appicharla. Railway System Safety. March 2012.

[7] Reinhold Bayerer, Tobias Herrmann, Thomas Licht, Josef Lutz, and Marco Feller. Model for power cycling lifetime of IGBT modules-various factors influencing lifetime. In *Proc. CIPS*, volume 11, page 13, 2008.

[8] Vishay BCcomponents. Aluminum Electrolytic Capacitors Power Ultra High Ripple Current Snap-In for Solar, 2017.

[9] U.M. Choi, F. Blaabjerg, S. Jørgensen, F. Iannuzzo, H. Wang, C. Uhrenfeldt, and S. Munk-Nielsen. Power cycling test and failure analysis of molded Intelligent Power IGBT Module under different temperature swing durations. *Microelectronics Reliability*, 64:403–408, September 2016.

[10] Henry Shu-hung Chung, Huai Wang, Frede Blaabjerg, and Michael Pecht. *Reliability of Power Electronic Converter Systems*. Institution of Engineering and Technology, 2015.

[11] L. F. Jr. Coffin. A Study of the Effects of Cyclic Thermal Stresses on a Ductile Metal,. *Transactions of the ASME*, (Vol. 76):pp. 931–950, 1954.

[12] Stephen D. Downing and D. F. Socie. Simple rainflow counting algorithms. *International journal of fatigue*, 4(1):31–40, 1982.

[13] Herbert C. Frey and Gero Nießen. *Monte Carlo Simulation - Quantitative Risikoanalyse Für Die Versicherungsindustrie*. Gerling Akademie Verlag, 2001.

[14] L. R. GopiReddy, L. M. Tolbert, and B. Ozpineci. Power Cycle Testing of Power Switches: A Literature Survey. *IEEE Transactions on Power Electronics*, 30(5):2465–2473, May 2015.

[15] Lakshmi Reddy GopiReddy, Leon M. Tolbert, Burak Ozpineci, and Joao OP Pinto. Rainflow algorithm-based lifetime estimation of power semiconductors in utility applications. *IEEE Transactions on Industry Applications*, 51(4):3368–3375, 2015.

[16] Hitachi. Thermal Equivalent Model of IGBT Modules, 2015.

[17] Infineon. Use of Power Cycling curves for IGBT 4, 2010.

[18] Winfried Kaindl. *Modellierung Höhenstrahlungsinduzierter Ausfälle in Halbleiterleistungsbauelementen.* PhD Thesis, Technische Universität München, 2005.

[19] Michael Köhler, Sven Jenne, Kurt Pötter, and Harald Zenner. *Zählverfahren Und Lastannahme in Der Betriebsfestigkeit.* Springer-Verlag, Berlin Heidelberg, 2012.

[20] B. Kroposki, B. Johnson, Y. Zhang, V. Gevorgian, P. Denholm, B. Hodge, and B. Hannegan. Achieving a 100% Renewable Grid: Operating Electric Power Systems with Extremely High Levels of Variable Renewable Energy. *IEEE Power and Energy Magazine*, 15(2):61–73, March 2017.

[21] Jie Liu and Norbert Henze. Reliability consideration of low-power grid-tied inverter for photovoltaic application. In *24th European Photovoltaic Solar Energy Conference, Hamburg, Germany, September*, pages 21–25, 2009.

[22] Josef Lutz, Heinrich Schlangenotto, Uwe Scheuermann, and Rik De Doncker. Reliability and Reliability Testing. In Josef Lutz, Heinrich Schlangenotto, Uwe Scheuermann, and Rik De Doncker, editors, *Semiconductor Power Devices: Physics, Characteristics, Reliability*, pages 489–581. Springer International Publishing, Cham, 2018.

[23] Josef Lutz, Heinrich Schlangenotto, Uwe Scheuermann, and Rik De Doncker. *Semiconductor Power Devices: Physics, Characteristics, Reliability.* Springer-Verlag, Berlin Heidelberg, 2011.

[24] K. Mainka, M. Thoben, and O. Schilling. Lifetime calculation for power modules, application and theory of models and counting methods. In *Proceedings of the 2011 14th European Conference on Power Electronics and Applications*, pages 1–8, August 2011.

[25] Samuel S. Manson. Behavior of materials under conditions of thermal stress. 1954.

[26] M. Matsuishi and T. Endo. Fatigue of metals subjected to varying stress. *Japan Society of Mechanical Engineers, Fukuoka, Japan*, 68(2):37–40, 1968.

[27] C. H. McInnes and P. A. Meehan. Equivalence of four-point and three-point rainflow cycle counting algorithms. *International Journal of Fatigue*, 30(3):547–559, 2008.

[28] A. Meyna and B. Pauli. *Taschenbuch Der Zuverlässigkeitstechnik: Quantitative Bewertungsverfahren*. Praxisreihe Qualitätswissen. Hanser, 2010.

[29] M.A. Miner. Cumulative Damage in Fatigue. *Journal of Applied Mechanics*, (3):159–164, 1945.

[30] L. M. Moore and H. N. Post. Five years of operating experience at a large, utility-scale photovoltaic generating plant. *Progress in Photovoltaics: Research and Applications*, 16(3):249–259, May 2008.

[31] Nippon Chemicon. General Descriptions of Aluminum Electrolytic Capacitors, nichicon. Technical report, Nippon Chemicon.

[32] Nippon Chemicon. Technical Note, Nippon Chemicon. Technical report, Nippon Chemicon.

[33] Milton Ohring. *Reliability and Failure of Electronic Materials and Devices*. Elsevier, 1998.

[34] Igor Rychlik. A new definition of the rainflow cycle counting method. *International journal of fatigue*, 9(2):119–121, 1987.

[35] Fred Schenkelberg. Calculating Capacitor Reliability. http://nomtbf.com/2014/01/calculating-capacity-reliability/, January 2014.

[36] H. Wang and F. Blaabjerg. Reliability of Capacitors for DC-Link Applications in Power Electronic Converters—An Overview. *IEEE Transactions on Industry Applications*, 50(5):3569–3578, September 2014.

[37] H. Wang, M. Liserre, F. Blaabjerg, P. de Place Rimmen, J. B. Jacobsen, T. Kvisgaard, and J. Landkildehus. Transitioning to Physics-of-Failure as a Reliability Driver in Power Electronics. *IEEE Journal of Emerging and Selected Topics in Power Electronics*, 2(1):97–114, March 2014.

[38] H. Wang, K. Ma, and F. Blaabjerg. Design for reliability of power electronic systems. In *IECON 2012 - 38th Annual Conference on IEEE Industrial Electronics Society*, pages 33–44, October 2012.

[39] Christoph Weiß. *Höhenstrahlungsresistenz von Silizium-Hochleistungsbauelementen*. PhD Thesis, Technische Universität München, 2015.

[40] L. Yang, P. A. Agyakwa, and C. M. Johnson. Physics-of-Failure Lifetime Prediction Models for Wire Bond Interconnects in Power Electronic Modules. *IEEE Transactions on Device and Materials Reliability*, 13(1):9–17, March 2013.

[41] S. Yang, A. Bryant, P. Mawby, D. Xiang, L. Ran, and P. Tavner. An Industry-Based Survey of Reliability in Power Electronic Converters. *IEEE Transactions on Industry Applications*, 47(3):1441–1451, May 2011.

[42] Shaoyong Yang, Dawei Xiang, Angus Bryant, Philip Mawby, Li Ran, and Peter Tavner. Condition Monitoring for Device Reliability in Power Electronic Converters: A Review. *IEEE Transactions on Power Electronics*, 25(11):2734–2752, November 2010.

[43] Y. Zhang, H. Wang, Z. Wang, Y. Yang, and F. Blaabjerg. Impact of lifetime model selections on the reliability prediction of IGBT modules in modular multilevel converters. In *2017 IEEE Energy Conversion Congress and Exposition (ECCE)*, pages 4202–4207, October 2017.

[44] ZVEI. Handbook for Robustness Validation of Semiconductor Devices in Automotive Applications (3rd edition). https://www.zvei.org/en/press-media/publications/handbook-for-robustness-validation-of-semiconductor-devices-in-automotive-applications-3rd-edition/, 2015.